




Distinct metabolic programs established in the thymus control effector functions of $\gamma\delta$ T cell subsets in tumor microenvironments

Noella Lopes^{1,8}, Claire McIntyre^{2,8}, Stefania Martin^{3,8}, Mathilde Raverdeau^{4,8}, Nital Sumaria³, Ayano C. Kohlgruber², Gina J. Fiala¹, Leandro Z. Agudelo⁵, Lydia Dyck⁴, Harry Kane^{2,4}, Aaron Douglas⁴, Stephen Cunningham⁴, Hannah Prendeville⁴, Roisin Loftus⁴, Colleen Carmody², Philippe Pierre^{6,7}, Manolis Kellis⁵, Michael Brenner², Rafael J. Argüello⁶, Bruno Silva-Santos^{1,8}, Daniel J. Pennington^{3,8}  and Lydia Lynch^{2,4,8}

Metabolic programming controls immune cell lineages and functions, but little is known about $\gamma\delta$ T cell metabolism. Here, we found that $\gamma\delta$ T cell subsets making either interferon- γ (IFN- γ) or interleukin (IL)-17 have intrinsically distinct metabolic requirements. Whereas IFN- γ ⁺ $\gamma\delta$ T cells were almost exclusively dependent on glycolysis, IL-17⁺ $\gamma\delta$ T cells strongly engaged oxidative metabolism, with increased mitochondrial mass and activity. These distinct metabolic signatures were surprisingly imprinted early during thymic development and were stably maintained in the periphery and within tumors. Moreover, pro-tumoral IL-17⁺ $\gamma\delta$ T cells selectively showed high lipid uptake and intracellular lipid storage and were expanded in obesity and in tumors of obese mice. Conversely, glucose supplementation enhanced the antitumor functions of IFN- γ ⁺ $\gamma\delta$ T cells and reduced tumor growth upon adoptive transfer. These findings have important implications for the differentiation of effector $\gamma\delta$ T cells and their manipulation in cancer immunotherapy.

T cells engage specific metabolic pathways to support their differentiation, proliferation and function^{1,2}. Whereas naive $\alpha\beta$ T cells oxidize glucose-derived pyruvate via oxidative phosphorylation (OXPHOS) or fatty acid oxidation (FAO) to generate ATP, most effector $\alpha\beta$ T cells engage in aerobic glycolysis ('Warburg effect'), that is the conversion of glucose to lactate, to strengthen cell growth and proliferation³. On the other hand, while aerobic glycolysis is required for optimal $\alpha\beta$ T cell effector function^{4,5}, tumor cells heavily consume glucose in the tumor microenvironment (TME), which has a dramatic impact on cytokine production by T cells and hampers tumor immunity^{5,6}. There is therefore great interest in understanding how metabolism-based interventions could inhibit tumor metabolism while promoting effective antitumor immunity for improved immunotherapeutic outcomes⁷.

$\gamma\delta$ T cells represent a promising immune population for next-generation cancer immunotherapies^{8,9}. Since they are not MHC-restricted nor dependent on neoantigen recognition, $\gamma\delta$ T cells constitute a complementary layer of antitumor immunity to their $\alpha\beta$ T cell counterparts¹⁰. In fact, many properties of $\gamma\delta$ T cells, including sensing of 'stress-inducible' changes and very rapid effector responses, align best with innate immunity, or 'lymphoid stress-surveillance'¹¹, although in some instances they display adaptive-like behavior and profound shaping of their T cell receptor (TCR) repertoires^{12,13}.

The effector functions of murine $\gamma\delta$ T cells are dominated by the production of two key cytokines, IL-17 and IFN- γ . Beyond

contributions to immune responses against pathogens, the provision of these two cytokines by $\gamma\delta$ T cells is important in many (patho) physiological contexts, such as maintenance of tissue homeostasis^{14,15}, autoimmunity¹⁶ and cancer⁸. IL-17 and IFN- γ are mostly produced by distinct $\gamma\delta$ T cell subsets that, unlike their CD4⁺ T cell counterparts, typically acquire their effector functions during thymic development^{17,18}. Thymic $\gamma\delta$ T cell progenitors, driven by signals including those stemming from the T cell receptor (TCR), split into a CD27⁺ (and CD45RB⁺) branch that makes IFN- γ but not IL-17, and a CD27⁻ (and CD44^{hi}) pathway that selectively expresses IL-17 (refs. 17–21).

The IFN- γ –IL-17 dichotomy between effector $\gamma\delta$ T cell subsets is particularly relevant in cancer, since IFN- γ -producing $\gamma\delta$ T cells ($\gamma\delta^{\text{IFN}}$) are associated with tumor surveillance and regression, whereas IL-17-secreting $\gamma\delta$ T cells ($\gamma\delta^{17}$) promote primary tumor growth and metastasis, both in mice and in humans^{8,22}. However, the molecular cues that regulate the balance between such antagonistic $\gamma\delta$ T cell subsets in the TME remain poorly characterized. Given the strong impact of metabolic resources on antitumor $\alpha\beta$ T cell responses, here we have investigated the metabolic profiles of $\gamma\delta$ T cell subsets and how they might impact their activities in the TME. We find that $\gamma\delta^{\text{IFN}}$ cells are almost exclusively glycolytic, whereas $\gamma\delta^{17}$ cells are strongly dependent on mitochondrial and lipid oxidative metabolism. This metabolic dichotomy is established in the thymus during $\gamma\delta$ T cell development, and is maintained in

¹Instituto de Medicina Molecular João Lobo Antunes, Faculdade de Medicina, Universidade de Lisboa, Lisbon, Portugal. ²Brigham and Women's Hospital, Harvard Medical School, Boston, MA, USA. ³Blizard Institute, Barts and The London School of Medicine, Queen Mary University of London, London, UK.

⁴Trinity Biomedical Science Institute, Trinity College Dublin, Dublin, Ireland. ⁵MIT Computer Science and Artificial Intelligence Laboratory, Cambridge, MA, USA. ⁶Aix Marseille Université, CNRS, INSERM, CIML, Centre d'Immunologie de Marseille-Luminy, Marseille, France. ⁷Institute for Research in Biomedicine (iBiMED) and Ildio Pinho Foundation, Department of Medical Sciences, University of Aveiro, Aveiro, Portugal. ⁸These authors contributed equally: Noella Lopes, Claire McIntyre, Stefania Martin, Mathilde Raverdeau, Bruno Silva-Santos, Daniel J. Pennington, Lydia Lynch.  e-mail: d.pennington@qmul.ac.uk

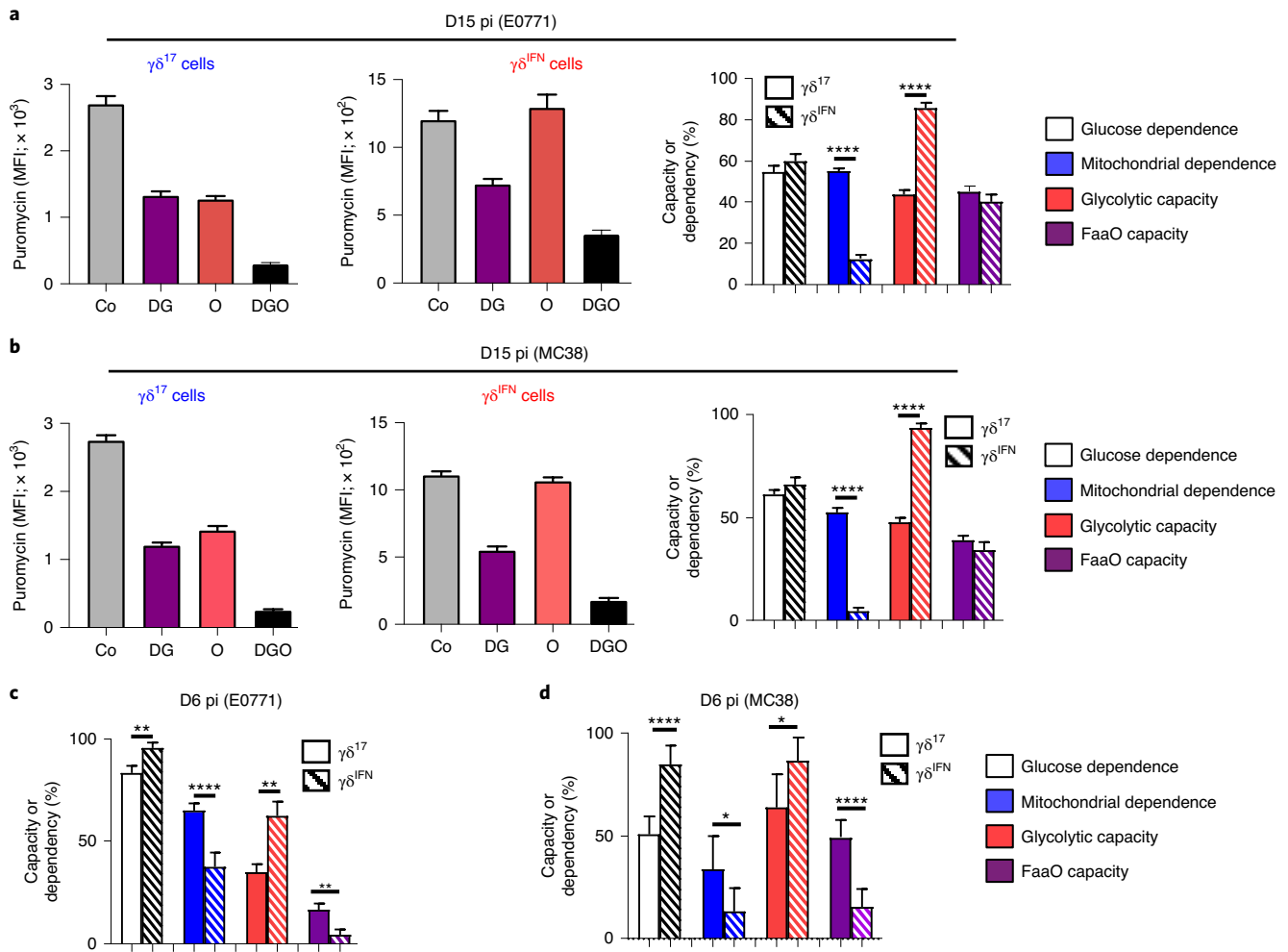


Fig. 1 | Intratumoral $\gamma\delta$ T cell subsets display distinct metabolic profiles. a–d, Puromycin mean fluorescence intensity (MFI) of tumor-infiltrating $\gamma\delta^{17}$ and $\gamma\delta^{IFN}$ cells extracted from E0771 breast (**a,c**) and MC38 colon (**b,d**) tumor-bearing mice analyzed using SCENITH in control conditions (Co) or after the addition of 2-DG, oligomycin (O) or both inhibitors (DGO). Graphs show the percentage of glucose dependence, mitochondrial dependence, glycolytic capacity and fatty acid and amino acid oxidation (FaaO) capacity of tumor-infiltrating $\gamma\delta^{17}$ and $\gamma\delta^{IFN}$ cells isolated either 6 d (**c**, glucose dependence ($P=0.0041$), mitochondrial dependence ($P<0.0001$), glycolytic capacity ($P=0.0014$) and fatty acid and amino acid oxidation ($P=0.0041$); **d**, glucose dependence ($P<0.0001$), mitochondrial dependence ($P=0.0345$), glycolytic capacity ($P=0.0189$) and fatty acid and amino acid oxidation ($P<0.0001$)) or 15 d (**a,b**: mitochondrial dependence ($P<0.0001$), glycolytic capacity ($P<0.0001$)) after cancer cell line injection. Data are representative of 3 independent experiments ($n=3$ mice per group in triplicates in each experiment). pi, post-injection. $\gamma\delta^{17}$ and $\gamma\delta^{IFN}$ T cells represent IL-17- and IFN- γ -producing $\gamma\delta$ T cells, respectively. Error bars show mean \pm s.e.m., * $P<0.05$; ** $P<0.01$; **** $P<0.0001$ using unpaired two-tailed Student's t -test.

peripheral lymphoid organs and within tumors in various experimental models of cancer. We further show that the provision of glucose or lipids has a major impact on the relative expansion and function of the two $\gamma\delta$ T cell subsets and that this can be used to enhance antitumor $\gamma\delta$ T cell responses.

Results

Intratumoral $\gamma\delta$ T cell subsets display distinct metabolic profiles.

The analysis of metabolic profiles of tumor-infiltrating $\gamma\delta$ lymphocytes ($\gamma\delta$ TILs) presented a major challenge: the low numbers that can be retrieved from tumor lesions in mice are largely incompatible with techniques such as Seahorse metabolic flux analysis. To overcome this difficulty, we used a newly developed protocol, SCENITH (Single Cell Metabolism by Profiling Translation Inhibition), which is a flow-cytometry-based method for profiling energy metabolism with single-cell resolution²³. This method is based on metabolism-dependent translation rates and puromycin's incorporation into nascent proteins (Extended Data Fig. 1). The use

of specific inhibitors allows the estimation of glucose dependence, mitochondrial dependence, glycolytic capacity and fatty acid and amino acid oxidation capacity. We employed SCENITH to analyze the metabolic profiles of $\gamma\delta$ TILs isolated from tumor lesions in well-established mouse models of breast (E0771) and colon (MC38) cancer. In both cancer models, and at both later (Fig. 1a,b) and earlier time points (Fig. 1c,d), we observed that $\gamma\delta^{IFN}$ cells had substantially higher glycolytic capacity, whereas $\gamma\delta^{17}$ cells were strongly dependent on mitochondrial activity (Fig. 1). These data, obtained in cancer models, prompted us to investigate the metabolic phenotypes of $\gamma\delta$ T cell subsets in multiple tissues at steady state.

Peripheral $\gamma\delta$ T cell subsets show different mitochondrial and metabolic phenotypes.

To explore the metabolic differences between $\gamma\delta$ T cell subsets in peripheral tissues, we analyzed mitochondria, given their central role in cellular metabolism. To distinguish between $\gamma\delta^{IFN}$ and $\gamma\delta^{17}$ cells, we used CD27 expression^{18–21}. CD27[−] $\gamma\delta$ ($\gamma\delta^{17}$) T cells displayed increased MitoTracker and

tetramethylrhodamine methyl ester (TMRE) staining in peripheral lymph nodes (LNs) compared to CD27⁺ $\gamma\delta$ ($\gamma\delta^{\text{IFN}}$) T cells, indicating higher mitochondrial mass (normalized to cell size) and mitochondrial membrane potential ($\Delta\Psi\text{m}$), respectively (Fig. 2a,b). These differences were retained upon activation and expansion in vitro (Extended Data Fig. 2). Importantly, the distinct mitochondrial phenotypes were also validated with another mitochondrial membrane potential dye, tetramethylrhodamine ethyl ester (TMRE), and were features of $\gamma\delta^{17}$ and $\gamma\delta^{\text{IFN}}$ cells ex vivo from multiple locations (Fig. 2c). In agreement with mitochondrial enrichment in $\gamma\delta^{17}$ cells, Seahorse metabolic-flux analysis of peripheral $\gamma\delta$ T cells showed higher levels of basal OXPHOS in $\gamma\delta^{17}$ cells, and conversely, increased basal levels of glycolysis in $\gamma\delta^{\text{IFN}}$ cells (Fig. 2d–f). These data were validated in independent experiments using SCENITH on splenic and LN $\gamma\delta$ T cell subsets (Fig. 2g).

To assess whether this metabolic dichotomy had an underlying transcriptional basis, we measured the mRNA levels of key mitochondrial and glycolysis-associated genes in purified peripheral $\gamma\delta^{17}$ and $\gamma\delta^{\text{IFN}}$ cells. We found systematic biases in gene expression that matched the differential metabolic programs (Fig. 2h,i). Of particular note is the clear-cut segregation of two master transcriptional regulators: nuclear respiratory factor 1 (*Nrf1*), which orchestrates mitochondrial DNA transcription^{24,25}, found to be enriched in $\gamma\delta^{17}$ cells (Fig. 2h), and *Myc* proto-oncogene, BHLH transcription factor (*Myc*), which controls glycolysis^{26,27}, that was highly overexpressed in $\gamma\delta^{\text{IFN}}$ cells (Fig. 2i). *Myc* expression was further validated using a Myc-green fluorescent protein (GFP) reporter mouse (Fig. 2j). These data collectively demonstrated that $\gamma\delta$ T cell subsets possess distinct mitochondrial and metabolic features in peripheral organs at steady state.

$\gamma\delta$ T cell subsets are metabolically programmed in the thymus.

We next aimed to understand when, during their differentiation, the metabolic differences between the two effector $\gamma\delta$ T cell subsets were established. Since most $\gamma\delta$ T cells are functionally preprogrammed in the thymus, we examined $\gamma\delta$ thymocyte subpopulations. Studies have identified sequential stages of thymic $\gamma\delta$ T cell progenitor development marked by CD24, CD44 and CD45RB¹⁹. Early CD24⁺ ($\gamma\delta^{24+}$) precursors downregulate CD24 to become a CD24⁻CD44⁻CD45RB⁻ ($\gamma\delta^{\text{TN}}$) population that generates cells committed to either IL-17 or IFN- γ expression, which display, respectively, CD44^{hi}CD45RB⁻ ($\gamma\delta^{17}$) and CD44⁺CD45RB⁺ ($\gamma\delta^{\text{IFN}}$) phenotypes (Extended Data Fig. 3). By using SCENITH, we found that, in both the adult (Fig. 3a) and newborn (Fig. 3b) thymus, these subsets showed the same metabolic dichotomy as in the periphery (Fig. 2g), although this was less distinct in $\gamma\delta$ thymocytes, likely due to the dynamic subset segregation process¹⁹.

To investigate any potential switching of metabolic programming during $\gamma\delta$ thymocyte development, we first compared early thymic $\gamma\delta$ progenitors with more mature subpopulations already committed to IL-17 or IFN- γ production. We found that $\gamma\delta^{24+}$ and $\gamma\delta^{\text{TN}}$ progenitors stained highly for TMRE, which was lost when $\Delta\Psi\text{m}$ was dissipated by the ionophore carbonyl cyanide-4-(trifluoromethoxy) phenylhydrazone (FCCP) (Fig. 3c,d). Although $\gamma\delta^{17}$ cells retained a high level of TMRE staining, $\gamma\delta^{\text{IFN}}$ cells showed a marked reduction in $\Delta\Psi\text{m}$, suggesting a metabolic switch away from OXPHOS (Fig. 3d). Moreover, imagestream analysis of $\gamma\delta^{17}$ cells stained with either MitoTracker or TMRE revealed large and active mitochondria, in contrast with $\gamma\delta^{\text{IFN}}$ cells, which displayed negligible staining for either dye (Fig. 3e), in line with our previous observations in peripheral subsets (Fig. 2a–c). Furthermore, Seahorse extracellular flux analysis showed that $\gamma\delta^{17}$ thymocytes have both higher maximal respiration potential and spare respiratory capacity than those of their $\gamma\delta^{\text{IFN}}$ counterparts (Fig. 3f,g). Thus, $\gamma\delta$ T cell subsets acquire distinct mitochondrial features during their acquisition of effector function in the thymus.

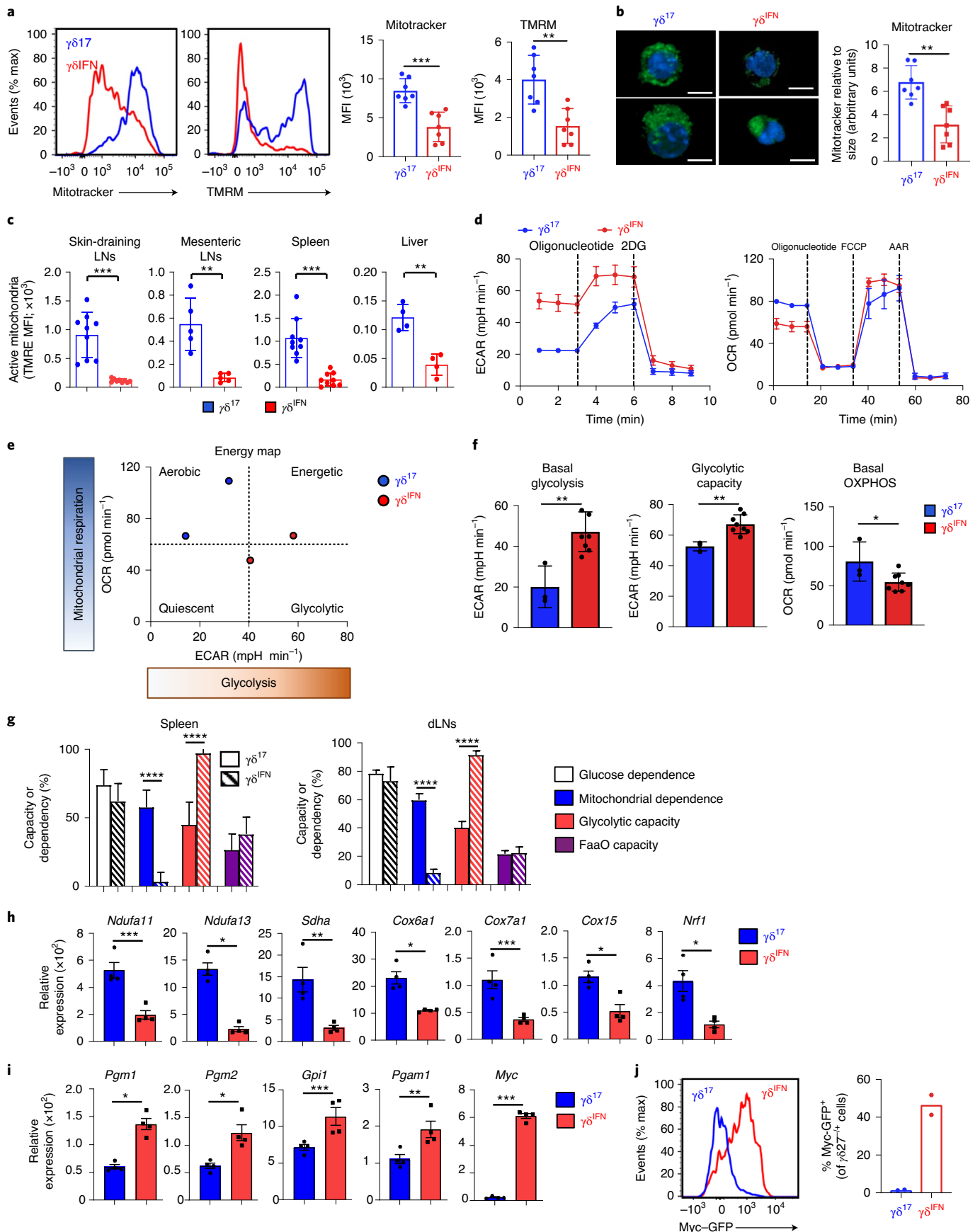
The adoption of divergent metabolic programs by thymic $\gamma\delta$ T cell subsets suggested that they could thrive under distinct metabolic environments. To begin to address this, we placed wild-type (WT) embryonic day 15 (E15) thymic lobes in organ culture for 7 days (E15 + 7-d fetal thymic organ cultures (FTOCs)) with media containing either low or high amounts of glucose (Fig. 3h). $\gamma\delta^{17}$ cells were readily detected in lower glucose conditions but failed to develop to normal numbers when glucose concentrations were raised. By contrast, $\gamma\delta^{\text{IFN}}$ cells were relatively enriched in high glucose conditions, as demonstrated by a significant decrease in the $\gamma\delta^{17}/\gamma\delta^{\text{IFN}}$ cell ratio (Fig. 3h). We next established E15 + 7-d FTOCs in the presence of the glycolysis inhibitor 2-deoxy-D-glucose (2-DG), and found increased numbers of $\gamma\delta^{17}$ cells and increased $\gamma\delta^{17}/\gamma\delta^{\text{IFN}}$ cell ratios (Fig. 3i). A similar result was observed in E15 + 7-d FTOC when cultured with fasentin, which blocks glucose uptake (Extended Data Fig. 4). By contrast, running E15 + 7-d FTOC in the presence of metformin, which reduces the efficiency of OXPHOS by inhibiting complex I of the electron transport chain, impaired $\gamma\delta^{17}$ cell generation and decreased the $\gamma\delta^{17}/\gamma\delta^{\text{IFN}}$ cell ratio (Fig. 3j). Collectively, these results suggest that the mitochondrial characteristics adopted by $\gamma\delta^{17}$ and $\gamma\delta^{\text{IFN}}$ cells during thymic development directly impact their ability to thrive in distinct metabolic environments.

Distinct mitochondrial activities underlie effector fate of thymic $\gamma\delta$ T cell precursors. We next aimed to investigate the association of distinct metabolic programs with the developmental divergence

Fig. 2 | Peripheral $\gamma\delta$ T cell subsets show different mitochondrial and metabolic phenotypes. **a**, Representative plots (left) and summary graphs (right) of the MFI of MitoTracker and tetramethylrhodamine methyl ester (TMRE) in $\gamma\delta^{27-}$ ($\gamma\delta^{17}$) and $\gamma\delta^{27+}$ ($\gamma\delta^{\text{IFN}}$) T cells ex vivo from LNs of C57BL/6 mice ($n=7$; data pooled from 2 experiments; MitoTracker $P=0.0003$; TMRE $P=0.0015$). **b**, Representative confocal images (left) of $\gamma\delta^{17}$ and $\gamma\delta^{\text{IFN}}$ cells stained with MitoTracker (green) and Hoechst 33342 (blue). Scale bar, 5 μm . Analysis of MitoTracker staining relative to cell size (right) in $\gamma\delta^{17}$ and $\gamma\delta^{\text{IFN}}$ cells ex vivo. Relative MitoTracker was calculated by dividing the MFI of MitoTracker by the MFI of FSC-A and multiplying by 100 ($n=7$, data pooled from 2 independent experiments; $P=0.0012$). **c**, TMRE MFI of $\gamma\delta^{17}$ and $\gamma\delta^{\text{IFN}}$ cells from skin-draining LNs, mesenteric LNs, spleen and liver of WT mice. Data are representative of 3 independent experiments ($n=3$ mice per group and experiment; sdLN $P=0.0003$; mLN $P=0.0095$; spleen $P=0.0001$; liver $P=0.0016$). **d**, Seahorse extracellular flux analysis of extracellular acidification rate (ECAR) and oxygen consumption rate (OCR) of $\gamma\delta^{17}$ and $\gamma\delta^{\text{IFN}}$ cells (expanded in vitro) from LNs ($\gamma\delta^{17}$ $n=2$, $\gamma\delta^{\text{IFN}}$ $n=5$, data are representative of 3 independent experiments). **e**, Energy map showing ECAR versus OCR of $\gamma\delta^{17}$ and $\gamma\delta^{\text{IFN}}$ cells. Each symbol represents average basal metabolism. **f**, Basal glycolytic rate, glycolytic capacity and basal OXPHOS of $\gamma\delta^{17}$ ($n=3$) and $\gamma\delta^{\text{IFN}}$ ($n=8$) cell subsets (data pooled from 2 independent experiments; basal glycolysis $P=0.0029$; glycolytic capacity $P=0.0042$; basal OXPHOS $P=0.0339$). **g**, Percentage of glucose dependence, mitochondrial dependence, glycolytic capacity and fatty acid and amino acid oxidation capacity of $\gamma\delta^{17}$ and $\gamma\delta^{\text{IFN}}$ cells from spleen and draining lymph nodes (dLNs). Data are representative of 3 independent experiments ($n=3$ mice in triplicates per group and per experiment). **h,i**, OXPHOS-related genes (*Ndufa11*, $P=0.0009$; *Ndufa13*, $P=0.0214$; *Sdha*, $P=0.0027$; *Cox6a1*, $P=0.0235$; *Cox7a1*, $P=0.0002$; *Cox15*, $P=0.0204$; *Nrf1*, $P=0.0248$) and glycolysis-related genes (*Pgm1*, $P=0.0226$; *Pgm2*, $P=0.0514$; *Gpi1*, $P=0.0003$; *Pgam1*, $P=0.0018$; *Myc*, $P=0.0002$) were measured by qPCR in purified $\gamma\delta^{17}$ ($n=4$) and $\gamma\delta^{\text{IFN}}$ ($n=4$) cells from spleen and dLN from WT mice. **j**, Representative plot (left) and percentages (right) of Myc-GFP⁺ $\gamma\delta^{17}$ and $\gamma\delta^{\text{IFN}}$ cells from LNs of Myc-GFP reporter mice ($n=2$). Error bars show mean \pm s.e.m. or s.d., * $P<0.05$; ** $P<0.01$; *** $P<0.001$, **** $P<0.0001$ using unpaired two-tailed Student's *t*-test.

of $\gamma\delta^{17}$ and $\gamma\delta^{IFN}$ cells in the thymus. Although the $\gamma\delta^{TN}$ population, that is the progenitor $\gamma\delta$ cell subset that immediately precedes the surface upregulation of either CD44 or CD45RB (marking commit-

ment to the IL-17 or IFN- γ pathways, respectively¹⁹) was predominantly TMRE^{hi}, we observed a fraction of cells with reduced TMRE staining that we reasoned might be transitioning to the TMRE^{lo}



state shown by $\gamma\delta^{\text{IFN}}$ cells (Fig. 3c). We further hypothesized that the metabolic status of $\gamma\delta^{\text{TN}}$ progenitors may predict their developmental fate. To test this, we sorted TMRE^{hi} and TMRE^{lo} cells from the $\gamma\delta^{\text{TN}}$ subset obtained from E15 + 7-d FTOC, and cultured them for 5 d on OP9-DL1 cells, which are known to support appropriate development of thymocytes²⁸. As predicted, virtually all cells from the TMRE^{lo} cultures upregulated CD45RB and entered the IFN- γ pathway (Fig. 4a); however, we were surprised that almost all cells from the TMRE^{hi} cultures entered the CD44^{hi} IL-17 pathway (Fig. 4a). This strongly suggests that $\gamma\delta^{\text{TN}}$ cells have already committed to an effector fate, and that this commitment associates with distinct mitochondrial activities.

To pursue this hypothesis further, we tested $\gamma\delta^{24+}$ progenitors that immediately precede the $\gamma\delta^{\text{TN}}$ subset; again, we observed a segregation of effector fate, with the majority of TMRE^{lo} $\gamma\delta^{24+}$ cells entering the IFN- γ pathway, and the majority of TMRE^{hi} $\gamma\delta^{24+}$ cells entering the IL-17 pathway (Fig. 4b). The observation that so few TMRE^{hi} $\gamma\delta^{24+}$ cells adopt an IFN- γ secreting fate again suggests that most $\gamma\delta^{24+}$ progenitors have already committed to subsequent effector function. Moreover, we found that differences in TMRE levels correlated with the known^{18,20,21} effector biases of V γ 1⁺ ($\gamma\delta^{\text{IFN}}$ -biased) and V γ 4⁺ ($\gamma\delta^{17}$ -biased) progenitors (Fig. 4c), and allowed TMRE-based segregation of effector fates using only V γ 4⁺ progenitors (Extended Data Fig. 5). Furthermore, among $\gamma\delta^{24+}$ thymocytes along the $\gamma\delta^{\text{IFN}}$ pathway, we observed a progressive downregulation of TMRE levels from $\gamma\delta^{\text{TN}}$ to CD44⁺CD45RB⁺ cells and finally $\gamma\delta^{\text{IFN}}$ cells (Fig. 4d).

Given that we and others^{20,21} have previously shown a key role for TCR signaling in $\gamma\delta^{\text{IFN}}$ thymocyte differentiation, we next asked if downregulation of TMRE levels associated with hallmarks of TCR signaling. Indeed, we found that low TMRE associated with high expression of CD73 (Fig. 4e), one of the best established markers of TCR signalling in $\gamma\delta$ T cell development^{20,28,29}. Moreover, in E15 thymic lobes, TMRE staining was reduced along with CD25 downregulation, which is another hallmark of (developmentally early) TCR $\gamma\delta$ signalling^{18,20,21} (Fig. 4f). Furthermore, at this E15 stage, the cells with the lowest TMRE staining were V γ 5⁺ progenitors (Fig. 4f) that are known to engage a Skint1-associated TCR ligand in the thymus and to uniformly commit to the IFN- γ pathway³⁰.

These lines of evidence suggested that $\gamma\delta$ progenitors receiving agonist TCR $\gamma\delta$ signals shift away from OXPHOS as indicated by their reduced $\Delta\Psi\text{m}$. To strengthen this point, we manipulated

TCR signals using agonist GL3 monoclonal antibody, which, as expected^{18,19}, promoted $\gamma\delta^{\text{IFN}}$ cell development while inhibiting the $\gamma\delta^{17}$ pathway in E17 + 6-d FTOC (Fig. 4g). Upon specifically sorting TMRE^{hi} $\gamma\delta^{24+}$ cells from E17 thymus and stimulating them with GL3 for 5 h, we found a subpopulation that downregulated CD24 together with TMRE levels, in a monoclonal-antibody-dose-dependent manner (Fig. 4h). These results strongly suggest that TCR signaling leads to $\Delta\Psi\text{m}$ downregulation as $\gamma\delta$ thymocytes differentiate into IFN- γ producers.

To gain further molecular resolution, we performed single-cell RNA-seq on TMRE^{lo} and TMRE^{hi} $\gamma\delta^{24+}$ cells from E15 + 2-d FTOCs (Extended Data Fig. 6a). Dimensionality reduction using UMAP (uniform manifold approximation and projection) showed that TMRE^{lo} cells clustered clearly away from TMRE^{hi} $\gamma\delta^{24+}$ cells (Fig. 4i), and the former were enriched in genes involved in the regulation of antigen receptor signaling (Fig. 4j). In support of the metabolic phenotypes observed ex vivo, genes associated with OXPHOS were enriched specifically in TMRE^{hi} $\gamma\delta^{24+}$ cells while genes involved in glucose metabolism were unregulated in TMRE^{lo} $\gamma\delta^{24+}$ cells (Extended Data Fig. 6b).

These data collectively demonstrate that metabolic status of thymic $\gamma\delta$ progenitors marks their developmental fate from a very early stage. Progenitors entering the IL-17 pathway display sustained high mitochondrial activity, whereas those in the IFN- γ pathway undergo a TCR-induced metabolic shift towards aerobic glycolysis. We next questioned how these intrinsic metabolic differences impacted the physiology of effector $\gamma\delta$ T cell subsets.

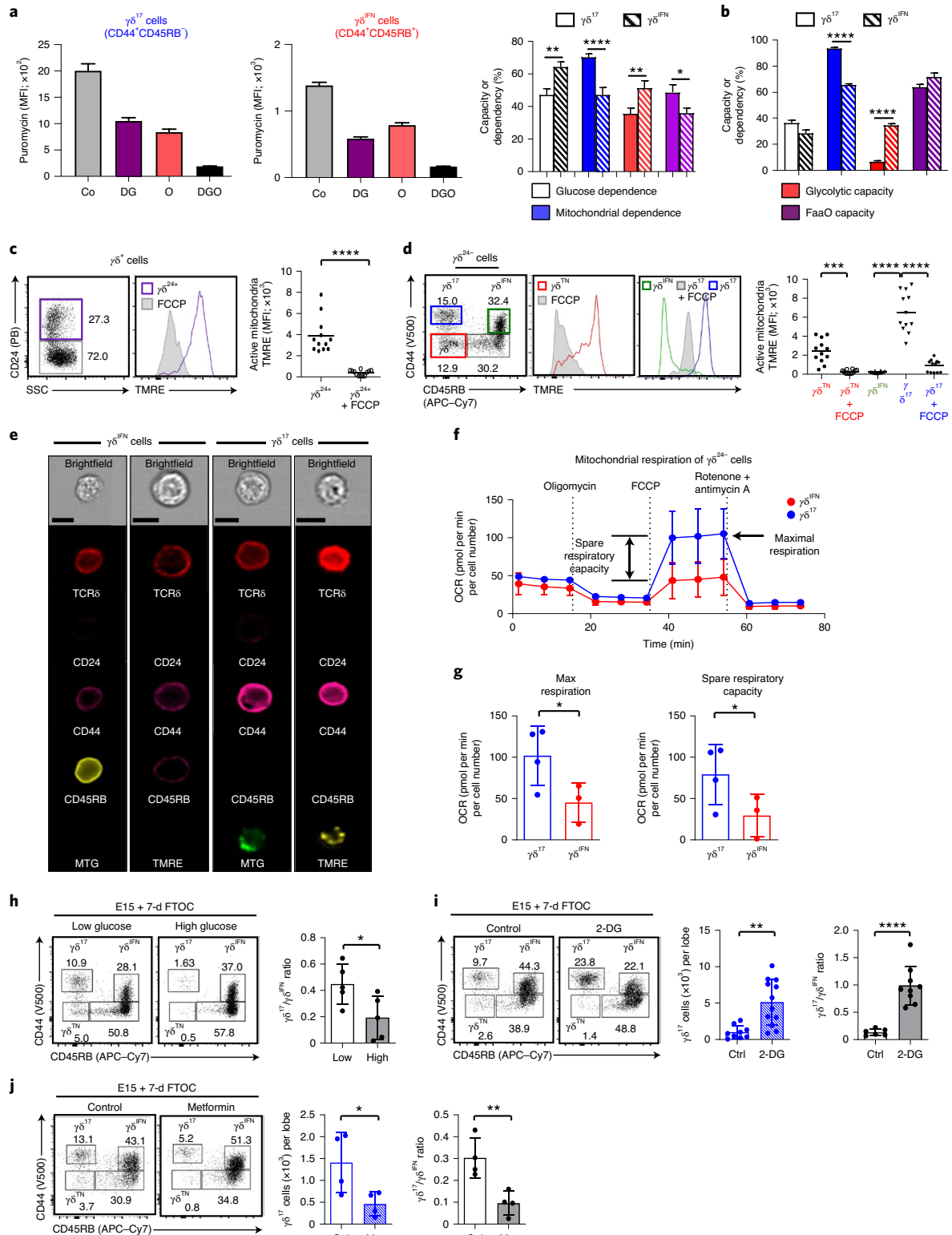
Enrichment of lipid storage and lipid metabolism in $\gamma\delta^{17}$ cells.

Having shown that, in stark contrast to $\gamma\delta^{\text{IFN}}$ cells, $\gamma\delta^{17}$ cell generation was reduced under high glucose concentrations (Fig. 3h), and enhanced upon inhibition of glycolysis (Fig. 3i) or glucose uptake (Extended Data Fig. 4), we questioned whether other metabolic resources might be important for $\gamma\delta^{17}$ cell physiology. To address this question, we took advantage of *Zbtb16*^{GFP} reporter mice to segregate $\gamma\delta^{17}$ and $\gamma\delta^{\text{IFN}}$ cells (*Zbtb16* encodes the transcription factor PLZF^{14,21,31}). We performed RNA sequencing (RNA-seq) of lymphoid and tissue-resident $\gamma\delta$ T cells sorted into PLZF⁺ ($\gamma\delta^{17}$) and PLZF⁻ ($\gamma\delta^{\text{IFN}}$) cells (Extended Data Fig. 7a). As expected, $\gamma\delta^{17}$ cells across tissues expressed *Il17a*, whereas *Il17f* was also expressed in tissue-resident $\gamma\delta^{17}$ cells (Fig. 5a). Different metabolic pathways

Fig. 3 | $\gamma\delta$ T cell subsets are metabolically programmed in the thymus. **a**, Puromycin MFI of $\gamma\delta^{17}$ (CD44^{hi}CD45RB⁻) and $\gamma\delta^{\text{IFN}}$ (CD44⁺CD45RB⁺) cells from WT adult thymus in resting conditions and after the addition of 2-DG, oligomycin or both. Histogram (right) shows the percentage of glucose dependency (white; $P=0.0029$), mitochondrial dependency (blue; $P<0.0001$), glycolytic capacity (red, $P=0.0018$) and fatty acid and amino acid oxidation capacity (purple, $P=0.0304$) of thymic $\gamma\delta^{17}$ and $\gamma\delta^{\text{IFN}}$ cells. Data are representative of two independent experiments ($n=5$ mice in triplicates per group and per experiment). **b**, Histograms show the percentage of glucose dependency (white), mitochondrial dependency (blue; $P<0.0001$), glycolytic capacity (red; $P<0.0001$) and fatty acid and amino acid oxidation capacity (purple) of $\gamma\delta^{17}$ and $\gamma\delta^{\text{IFN}}$ cells from WT newborn thymus (d3). Data are representative of three independent experiments ($n=6$ mice in triplicates per group and per experiment). **c**, Flow cytometry profile and TMRE MFI of thymic $\gamma\delta^{24+}$ precursors treated or not with FCCP ($P<0.0001$). Data are representative of three independent experiments (data points represent at least four lobes pooled per group and per experiment). **d**, Flow cytometry profiles and TMRE MFI of thymic $\gamma\delta^{\text{TN}}$ (CD44⁻CD45RB⁻), $\gamma\delta^{17}$ (CD44^{hi}CD45RB⁻) and $\gamma\delta^{\text{IFN}}$ (CD44⁺CD45RB⁺) cells treated or not with FCCP. $\gamma\delta^{\text{TN}}$ versus $\gamma\delta^{\text{TN}}$ + FCCP ($P=0.0002$), $\gamma\delta^{\text{IFN}}$ versus $\gamma\delta^{17}$ ($P<0.0001$), and $\gamma\delta^{17}$ versus $\gamma\delta^{17}$ + FCCP ($P<0.0001$). Data are representative of three independent experiments (data points represent at least four lobes pooled per group and per experiment). **e**, Imagestream analysis of $\gamma\delta^{17}$ and $\gamma\delta^{\text{IFN}}$ cells stained with either MitoTracker green or TMRE. Scale bar, 7 μm . Data are representative of two independent experiments. **f**, OCR of $\gamma\delta^{17}$ and $\gamma\delta^{\text{IFN}}$ cells from thymuses of 5-d-old B6 pups was measured by Seahorse extracellular flux analysis in real time under basal conditions and in response to indicated mitochondrial inhibitors. Data are representative of three independent experiments (pooled thymic lobes from $n>10$ mice per group per experiment). **g**, Histograms show maximal respiration potential ($P=0.0278$) and spare respiratory capacity ($P=0.0332$) by measuring OCR of $\gamma\delta^{17}$ and $\gamma\delta^{\text{IFN}}$ cells from thymuses of 5-d-old B6 pups. Data are representative of 3 independent experiments (pooled thymic lobes from $n>10$ mice per group per experiment). **h-j**, Flow cytometry profiles of thymic $\gamma\delta^{\text{TN}}$, $\gamma\delta^{17}$ and $\gamma\delta^{\text{IFN}}$ cells from 7-d FTOCs of E15 thymic lobes either with medium containing low (5 mM) or high (25 mM) glucose (**h**) or with or without 2-DG (**i**) or metformin (**j**). Histograms show the number of $\gamma\delta^{17}$ cells (2-DG $P=0.0013$; metformin $P=0.0426$) and $\gamma\delta^{17}/\gamma\delta^{\text{IFN}}$ cell ratio (glucose $P=0.0354$; 2-DG $P<0.0001$; metformin $P=0.0079$). Data are representative of two (**h**) or three (**i,j**) independent experiments (at least four lobes pooled per group per experiment). Error bars show mean \pm s.e.m. or s.d., * $P<0.05$, ** $P<0.01$, *** $P<0.001$, **** $P<0.0001$ using unpaired or paired two-tailed Student's *t*-test or one-way analysis of variance (ANOVA) test with Tukey's multiple-comparisons test.

were associated with lymphoid versus tissue-resident $\gamma\delta$ T cells. However, the genes common to $\gamma\delta^{17}$ cells across all tissues were related to lipid and mitochondrial metabolism, including glutamate transporter (*Slc1a1*), glucose/fatty acid metabolism (*Pdk4*), mitochondrial protein transport (*Ablim3*) and lipid metabolism (*Fabp1*, *Abdh5*, *Atp10a*). These data highlight genes associated with lipid metabolism as a common feature of $\gamma\delta^{17}$ T cells across tissues.

Consistent with this, LN $\gamma\delta^{17}$ cells had a higher neutral lipid content (assessed by LipidTOX staining) than $\gamma\delta^{\text{IFN}}$ cells (Fig. 5b). This differential lipid content was further increased upon activation with IL-1 β +IL-23 (Extended Data Fig. 7b), was associated with expression of IL-17A, IL-17F and ROR γ t (Extended Data Fig. 7c), and was observed across $\gamma\delta$ T cells from multiple tissues, with the notable exception of the skin (Fig. 5c), where $\gamma\delta$ T cells have been shown



to display specific mechanisms of tissue adaptation³². In particular, V γ 6⁺ $\gamma\delta$ T cells in the dermis are transcriptionally distinct from those in pLNs and display a highly activated but less proliferative phenotype. This tissue adaptation may alter the metabolic requirements of skin-resident $\gamma\delta$ T cells and $\gamma\delta$ T cells may adapt to utilize specific metabolites present within the skin³³.

Imaging analysis revealed that the increased LipidTOX staining was due to the accumulation of intracellular lipid droplets in $\gamma\delta^{17}$ cells (Fig. 5d,e). Lipid droplets store neutral lipids including triglycerides (TAGs) and cholesterol esters³⁴. The two $\gamma\delta$ T cell subsets had equivalent TAG content (Fig. 5f) but free cholesterol, as determined by filipin III staining, was higher in $\gamma\delta^{17}$ cells (Fig. 5g). We next questioned whether $\gamma\delta^{17}$ cells engaged in lipid uptake which could account for lipid storage. Using labeled palmitate (Bodipy-FL-C₁₆), we found that $\gamma\delta^{17}$ cells selectively took up lipids (Fig. 5h), which was further enhanced following activation (Extended Data Fig. 7d). Analysis of $\gamma\delta$ T cell cytokine production confirmed that the ability to take up palmitate was specific to IL-17 producers (Fig. 5i,j). Of note, V γ 4⁺ and V γ 6⁺ (V γ 1⁻V γ 4⁻) $\gamma\delta$ T cells showed a higher palmitate uptake than V γ 1⁺ cells (Fig. 5k). While V γ 6⁺ $\gamma\delta$ T cells primarily produce IL-17, V γ 4⁺ cells can produce either IFN- γ or IL-17^{18,19}. However, palmitate uptake was specific to V γ 4⁺ cells that produced IL-17 (Fig. 5l). Furthermore, $\gamma\delta^{17}$ cells also displayed higher uptake of fluorescently labeled cholesterol ester (Bodipy CholEsteryl FL-C₁₂) (Fig. 5m), emphasizing their ability to take up multiple types of lipids, including fatty acids and cholesterol.

These data demonstrate that $\gamma\delta^{17}$ cells have an exquisite capacity to take up and accumulate intracellular lipids, and display transcriptional signatures of enhanced lipid metabolism compared with $\gamma\delta^{IFN}$ cells.

High-fat diet promotes $\gamma\delta^{17}$ cell expansion and their accumulation in tumors. We next tested the effect of a lipid-rich, high-fat diet (HFD), on $\gamma\delta$ T cell subsets in vivo. Unlike mice fed a standard-fat diet (SFD), which alternate between using lipids or carbohydrates for fuel during light–dark cycles, respectively, mice fed an HFD had reduced respiratory exchange ratio (RER), illustrating a systemic metabolic switch to constantly burning lipids as the main fuel source. (Fig. 6a). We found that both the percentage and absolute number of LN $\gamma\delta$ T cells were increased during HFD (Fig. 6b), which was due to a specific increase in $\gamma\delta^{17}$ (but not $\gamma\delta^{IFN}$) cells (Fig. 6c,d).

Tumors are another site reported to be lipid-rich. To explore the effect of the lipid-rich tumor environment on $\gamma\delta^{17}$ cells, we employed the B16F10 melanoma model. In SFD mice, we found an enrichment of $\gamma\delta^{17}$ cells within the tumor compared with in draining LN (dLN) or spleen (Fig. 6e). These $\gamma\delta^{17}$ cells were also

enriched compared with $\gamma\delta^{IFN}$ cells (Fig. 6f). Given that $\gamma\delta^{17}$ cells were enriched in obese mice and in tumors, we next asked if obesity combined with the tumor model would further increase $\gamma\delta^{17}$ cells. Mice fed HFD exhibited enhanced tumor growth (Fig. 6g) and further increased percentages and numbers of tumor-infiltrating $\gamma\delta^{17}$ cells compared with the SFD group (Fig. 6h–j). These data demonstrate that a lipid-rich environment selectively accumulates $\gamma\delta^{17}$ cells but not $\gamma\delta^{IFN}$ cells in the tumor.

Given the preferential uptake of cholesterol by $\gamma\delta^{17}$ cells (Fig. 5i), we next investigated its effect on $\gamma\delta^{17}$ cell proliferation and function. We incubated purified $\gamma\delta^{27-}$ ($\gamma\delta^{17}$) cells with cholesterol-loaded cyclodextrin (CLC), which we found to promote $\gamma\delta^{27-}$ cell proliferation when compared with control culture conditions (Fig. 6k). To determine its impact on tumor growth in vivo, we injected CLC-pretreated (or control) $\gamma\delta^{17}$ cells twice (within 2 d) into subcutaneous E0771 tumors (as established in Fig. 1b), which allow local T cell delivery. Strikingly, $\gamma\delta^{17}$ cells pretreated with CLC substantially enhanced tumor growth (Fig. 6l–n).

Conversely, we also tested the effect of reducing lipids in vivo, by injected orlistat, which inhibits lipases and thus prevents uptake of dietary fat, into B16F10-tumor-bearing mice. Mice injected with orlistat exhibited reduced body weight and tumor growth compared to vehicle-treated mice (Extended Data Fig. 7a,b). Importantly, these mice showed decreased numbers of tumor-infiltrating $\gamma\delta^{17}$ cells, which had lower neutral lipid content (Extended Data Fig. 7c,d). Together, these data show that lipid-rich environments promote the selective expansion of $\gamma\delta^{17}$ cells that support tumor growth.

Glucose supplementation enhances antitumor functions of $\gamma\delta^{IFN}$ cells. We next aimed to use the knowledge gathered in this study to boost antitumor $\gamma\delta$ T cell responses, which are known to rely on $\gamma\delta^{IFN}$ cells^{8,22}. Given our data showing that glucose promotes the development of $\gamma\delta^{IFN}$ over $\gamma\delta^{17}$ cells in the thymus (Fig. 3h,i), and the higher glycolytic capacity of $\gamma\delta^{IFN}$ cells in peripheral organs (Fig. 2g) and also within tumors (Fig. 1b–e), we hypothesized that glucose supplementation would enhance $\gamma\delta^{IFN}$ cell functions. Further supporting this hypothesis, we found that intratumoral $\gamma\delta^{IFN}$ cells preferentially took up fluorescently labeled glucose (2-NDBG) when compared with $\gamma\delta^{17}$ TILs (Fig. 7a).

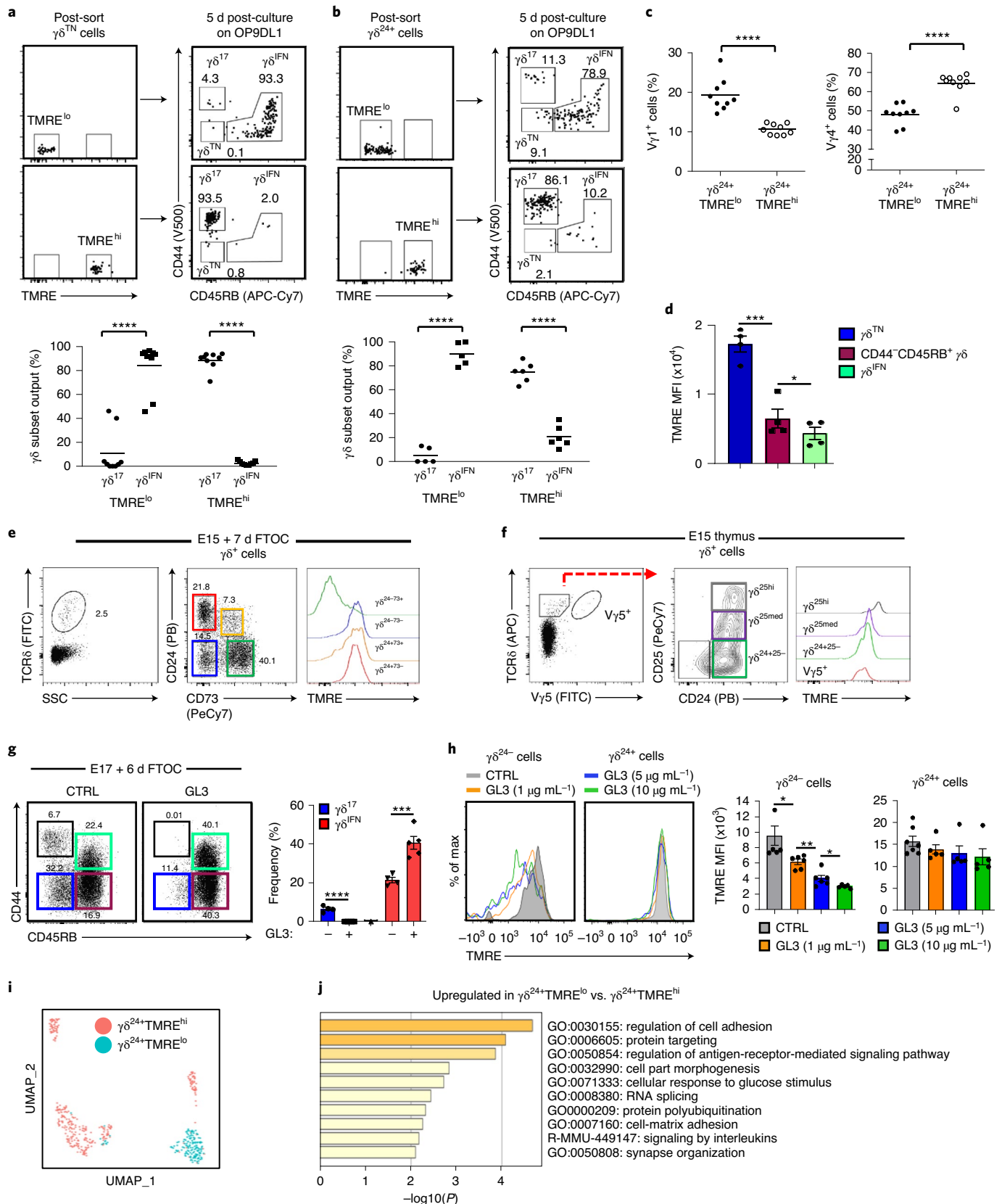
We first tested the impact of glucose on $\gamma\delta^{17}$ and $\gamma\delta^{IFN}$ cell functions in vitro. We cultured purified $\gamma\delta^{27-}$ ($\gamma\delta^{17}$) or $\gamma\delta^{27+}$ ($\gamma\delta^{IFN}$) cells in standard culture conditions containing a low dose of glucose (5 mM) or in high glucose (50 mM). We found high glucose to be detrimental to $\gamma\delta^{17}$ cells (Extended Data Fig. 8), in stark contrast to $\gamma\delta^{IFN}$ cells. Indeed, supplementation with high glucose augmented (whereas provision of 2-DG reduced) the percentage and numbers of $\gamma\delta^{IFN}$ cells (Fig. 7b), with parallel effects on their proliferation

Fig. 4 | Distinct mitochondrial activities underlie effector fate of thymic $\gamma\delta$ T cell progenitors. **a,b**, Flow cytometry profiles and percentage of thymic $\gamma\delta^{17}$ and $\gamma\delta^{IFN}$ cell output from sorted TMRE^{lo} and TMRE^{hi} $\gamma\delta^{TN}$ cells (**a**) or $\gamma\delta^{24+}$ cells (**b**) after 5-d culture on OP9DL1 cells. Data are representative of 3 independent experiments ($n=4$ mice pooled per group per experiment). **c**, Percentage of V γ 1⁺ and V γ 4⁺ cells in TMRE^{lo} and TMRE^{hi} $\gamma\delta^{24+}$ progenitors. V γ 1⁺ TMRE^{lo} versus TMRE^{hi} $P < 0.0001$ and V γ 4⁺ TMRE^{lo} versus TMRE^{hi} $P < 0.0001$. Data are representative of 3 independent experiments (cells sorted from $n=4$ mice pooled per group per experiment). **d**, TMRE MFI of thymic $\gamma\delta^{TN}$ (CD44⁻CD45RB⁻), CD24⁻CD44⁻CD45RB⁺ $\gamma\delta$ T cells and $\gamma\delta^{IFN}$ cells (CD44⁺CD45RB⁺) from 6-d FTOCs of E17 B6 thymic lobes; $\gamma\delta^{TN}$ versus CD44⁻CD45RB⁺ $\gamma\delta$ T cells ($P=0.002$), and CD44⁻CD45RB⁺ $\gamma\delta$ T cells versus $\gamma\delta^{IFN}$ cells ($P=0.0301$). Data are representative of 2 independent experiments ($n=4$ thymi pooled per point per group and per experiment). **e**, TMRE staining in CD24⁻CD73⁺, CD24⁻CD73⁻, CD24⁺CD73⁺ and CD24⁺CD73⁻ $\gamma\delta$ T cells from 7-d FTOCs of E15 B6 thymic lobes. **f**, TMRE staining in CD25⁻CD24⁺ ($\gamma\delta^{24+}$ cells), CD25^{med}, CD25^{hi} and V γ 5⁺ $\gamma\delta$ progenitors from E15 thymus. **g**, Flow cytometry profiles of thymic $\gamma\delta^{TN}$, $\gamma\delta^{17}$ and $\gamma\delta^{IFN}$ cells from 6-d FTOCs of E17 B6 thymic lobes stimulated or not with anti-TCR δ monoclonal antibody (GL3; 1 $\mu\text{g ml}^{-1}$). The graph shows the percentage of $\gamma\delta^{17}$ (–GL3 versus +GL3; $P < 0.0001$) and $\gamma\delta^{IFN}$ (–GL3 versus +GL3; $P=0.0002$) cells in each condition. Data are representative of 2 independent experiments ($n=4$ thymi pooled per point per group and per experiment). **h**, FACS-sorted $\gamma\delta^{24+}$ TMRE^{hi} cells from E17 thymi were cultured (or not) for 5 h with different concentrations (as indicated) of anti-TCR δ monoclonal antibody (GL3). TMRE levels were analyzed by flow cytometry in $\gamma\delta^{24-}$ and $\gamma\delta^{24+}$ cells. CTRL vs GL3 (1 $\mu\text{g ml}^{-1}$), $P=0.0271$; GL3 (1 $\mu\text{g ml}^{-1}$) versus GL3 (5 $\mu\text{g ml}^{-1}$), $P=0.0021$ and GL3 (5 $\mu\text{g ml}^{-1}$) versus GL3 (10 $\mu\text{g ml}^{-1}$), $P=0.0475$. Data are representative of 2 independent experiments ($n=3$ mice pooled per group per experiment). **i**, Single-cell RNA-seq clustering of TMRE^{lo} and TMRE^{hi} $\gamma\delta^{24+}$ cells from E15 + 2-d FTOCs using UMAP. **j**, Gene Ontology term analysis of genes upregulated in TMRE^{lo} versus TMRE^{hi} $\gamma\delta^{24+}$ cells shown in **i**. Error bars show mean \pm s.d., * $P < 0.05$, ** $P < 0.01$, *** $P < 0.001$, **** $P < 0.0001$ using unpaired two-tailed Student's *t*-test.

(Fig. 7c) and on the levels of expression of both IFN- γ (Fig. 7d) and its master transcriptional regulator²¹, T-bet (Fig. 7e).

To specifically address the importance of aerobic glycolysis for $\gamma\delta^{\text{IFN}}$ cells, we cultured $\gamma\delta^{\text{IFN}}$ cells with galactose (compared with

glucose), since cells grown in galactose enter the pentose phosphate pathway instead of using aerobic glycolysis^{35,36}. We observed a reduction in the percentage and absolute numbers of $\gamma\delta^{\text{IFN}}$ cells (Fig. 7f), as well as in their IFN- γ (Fig. 7g) and T-bet (Fig. 7h)



expression levels, thus establishing that aerobic glycolysis is required for optimal IFN- γ production by $\gamma\delta^{\text{IFN}}$ cells.

Next we asked if the cytotoxic function of $\gamma\delta^{\text{IFN}}$ cells was also enhanced by glucose supplementation. For this, we cocultured $\gamma\delta^{\text{IFN}}$ cells that were previously supplemented (or not) with a high dose of glucose with E0771 breast cancer cells at different effector:target (E:T) ratios. 'Glucose-enhanced' $\gamma\delta^{\text{IFN}}$ cells displayed substantially higher cytotoxic potency against the cancer cells than did the respective controls at each E:T ratio (Fig. 7i).

As $\gamma\delta$ T cells are actively being pursued in the clinic as an adoptive cell therapy for cancer⁸, we tested whether we could use glucose supplementation to enhance the antitumor functions of $\gamma\delta^{\text{IFN}}$ cells in vivo, in an adoptive-cell-transfer setting. Purified $\gamma\delta^{\text{IFN}}$ cells were cultured in the presence or absence of high-dose glucose for 5 h, washed and injected twice (within 2 d) into the tumor site. While control $\gamma\delta^{\text{IFN}}$ cells produced a small yet significant reduction in tumor size, glucose substantially augmented the antitumor effects of $\gamma\delta^{\text{IFN}}$ cells, essentially inhibiting tumor growth (from the time of injection) within the time window analyzed (Fig. 7j,k). These data reveal a new, metabolism-based means to enhance the antitumor functions of $\gamma\delta$ T cells that could be explored for adoptive cell immunotherapy of cancer.

Discussion

Metabolism dysregulation is viewed as an immune evasion strategy in cancer. To overcome it, and thus enable antitumor immune responses, it is critical to understand immune cell metabolism and its interplay with tumor cells in the TME. Although our knowledge on $\alpha\beta$ T cell metabolism has increased significantly^{1,3,37}, little is known about $\gamma\delta$ T cells. Here, we identified a metabolic dichotomy between the main effector $\gamma\delta$ T cell subsets that play opposing roles in cancer immunity^{8,22}. Whereas antitumoral $\gamma\delta^{\text{IFN}}$ cells are almost exclusively glycolytic, protumoral $\gamma\delta^{17}$ cells require mitochondrial metabolism; and their activities within tumors can be promoted by glucose or lipid metabolism, respectively.

Unexpectedly, the metabolic dichotomy of $\gamma\delta$ T cell subsets is established early during thymic development, which contrasts with the peripheral metabolic (re)programming of effector $\alpha\beta$ T cells. Naive $\alpha\beta$ T cells require activation to undergo rewiring of cellular metabolism, namely the transition from OXPHOS to aerobic glycolysis, through which glucose is fermented into lactate rather than oxidized in mitochondria³. Furthermore, depending on metabolic cues in the tissue or during immune challenge, naive T cells are pushed toward $T_{\text{H}1}$, $T_{\text{H}2}$, $T_{\text{H}17}$ or T_{reg} fates, dependent on intrinsic metabolic pathways engaged outside the thymus. By contrast, we show that an equivalent metabolic shift occurs in early thymic $\gamma\delta$ progenitors as

they commit to the IFN- γ pathway, seemingly as a result of strong TCR $\gamma\delta$ signaling. Indeed, analysis of various hallmarks of TCR signalling suggest that $\gamma\delta$ progenitors receiving agonist TCR $\gamma\delta$ signals shifted away from OXPHOS as indicated by their reduced $\Delta\Psi_{\text{m}}$. Moreover, upon TCR (GL3 monoclonal antibody) stimulation, a small population of $\gamma\delta$ progenitors downregulated CD24 together with $\Delta\Psi_{\text{m}}$ (TMRE), thus associating strong TCR $\gamma\delta$ signaling in the $\gamma\delta^{\text{IFN}}$ developmental pathway with metabolic reprogramming. This draws a parallel with $\alpha\beta$ T cell activation, during which early TCR signaling is required for induction of aerobic glycolysis³⁸. This acts as a switch for *Myc* mRNA (and protein) expression, such that strength of TCR stimulus determines the frequency of T cells that transcribe *Myc* mRNA³⁶. The common denominator of the metabolic switches in effector $\gamma\delta$ and $\alpha\beta$ T cells may thus be upregulation of *Myc*, which is required for transcription of genes encoding glycolytic enzymes^{26,27}. Indeed, our data show a striking enrichment of *Myc* (mRNA and protein) in $\gamma\delta^{\text{IFN}}$ cells compared with $\gamma\delta^{17}$ cells. On the other hand, the sustained dependence of $\gamma\delta^{17}$ cells on mitochondrial OXPHOS is in line with that recently reported for their functional $\alpha\beta$ T cell equivalents, $T_{\text{H}17}$ cells³⁹. Of note, IL-17-producing type 3 innate lymphoid cells (ILC3) were recently shown to require both glycolysis and mitochondrial-derived reactive oxygen species for activation⁴⁰, but a direct comparison with type 1 ILCs is still missing.

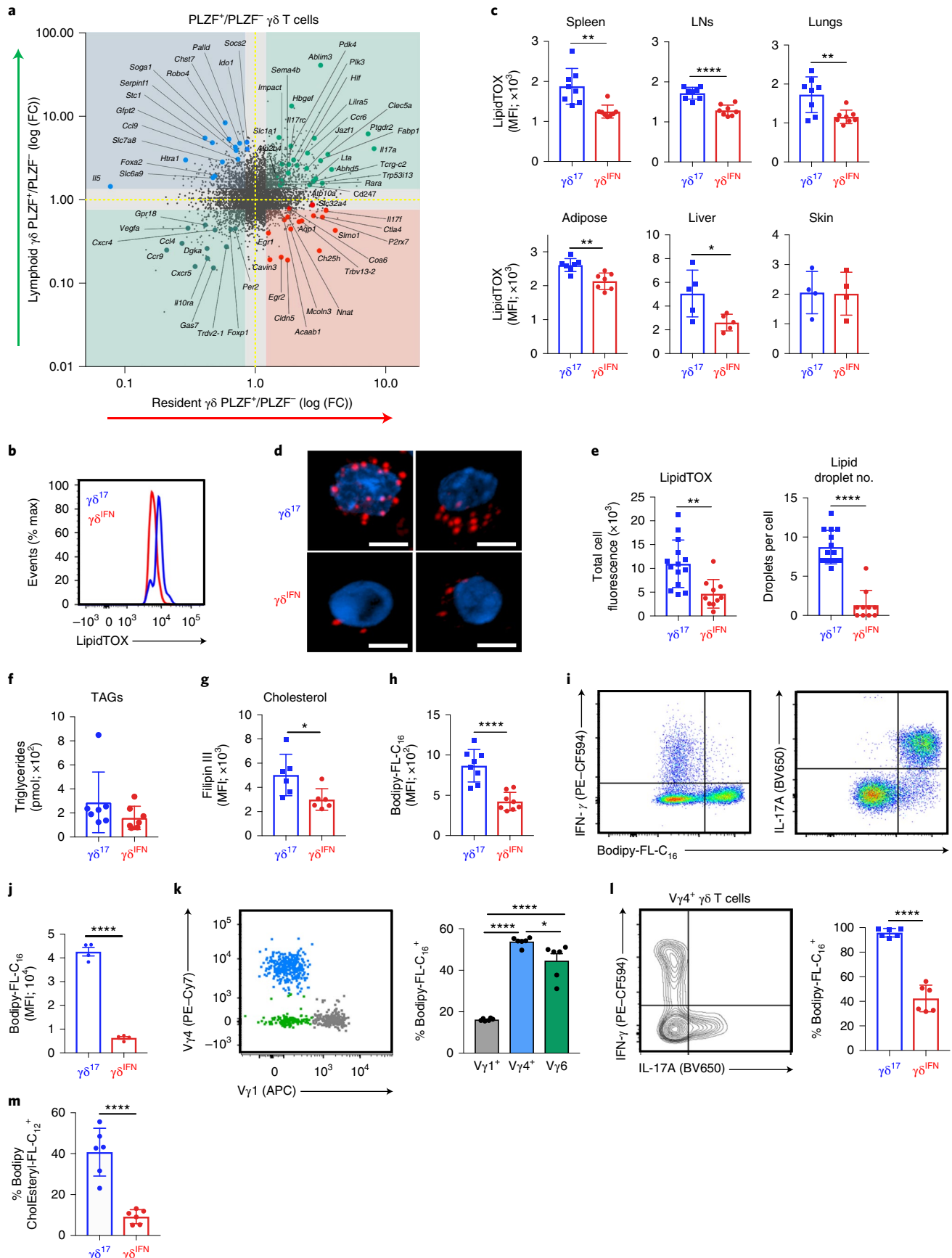
The concept of TCR signaling playing a key role in the metabolic programming of $\gamma\delta$ T cell subsets builds upon, but provides a novel perspective to, previous models of their thymic development. Thus, the unequivocal dependence on strong TCR signals for $\gamma\delta^{\text{IFN}}$ cell differentiation^{20,30} may be linked to a required metabolic shift to aerobic glycolysis. Moreover, the detrimental impact of agonist TCR signals on $\gamma\delta^{17}$ cell development may be due to metabolic conflict with their OXPHOS requirements, documented by our FTOC experiments using specific inhibitors. Importantly, these distinct metabolic phenotypes are maintained in peripheral $\gamma\delta$ T cell subsets, which is consistent with and expands our previous epigenetic and transcriptional analyses^{41,42}.

We were particularly interested in investigating the metabolic properties of peripheral $\gamma\delta$ T cell subsets once they infiltrated tumor lesions, for which we employed three experimental models of cancer (melanoma, breast and colon). Critically, we found that the dichotomy between $\gamma\delta^{17}$ and $\gamma\delta^{\text{IFN}}$ subsets was preserved in the TME, which enabled metabolic interventions that may have therapeutic potential. In fact, while $\gamma\delta$ T cell infiltration is largely perceived to associate with favorable prognosis in cancer patients⁴³, recent clinical data have suggested that, in agreement with mouse experimental systems²², human $\gamma\delta^{17}$ versus $\gamma\delta^{\text{IFN}}$ cell subsets have antagonistic prognostic values⁸. Thus, improvement in the thera-

Fig. 5 | $\gamma\delta^{17}$ cells show higher lipid uptake and lipid droplet content than $\gamma\delta^{\text{IFN}}$ cells. **a**, Quadrant plot of genes upregulated in bulk RNA-seq of tissue-resident PLZF⁺ $\gamma\delta$ T cells (lower right), lymphoid PLZF⁺ $\gamma\delta$ T cells (upper left), PLZF⁺ $\gamma\delta$ T cells from all tissues (upper right) or PLZF⁻ $\gamma\delta$ T cells from all tissues (lower left). Cells were isolated from PLZF-GFP (*Zbtb16*^{GFP}) mice. FC, fold change. **b**, Representative histogram of neutral lipid staining (LipidTOX) in $\gamma\delta^{17}$ (CD27⁻) and $\gamma\delta^{\text{IFN}}$ (CD27⁺) cells from LNs ex vivo. **c**, LipidTOX MFI in $\gamma\delta^{17}$ and $\gamma\delta^{\text{IFN}}$ cells from spleen ($P=0.0021$), LNs ($P<0.0001$), lungs ($P=0.0043$), adipose ($P=0.0018$), liver ($P=0.031$) and skin ($P=0.9442$) ($n=5-8$, data pooled from 2 independent experiments). **d**, Confocal imaging of $\gamma\delta^{17}$ and $\gamma\delta^{\text{IFN}}$ cells expanded in vitro and stained with LipidTOX (red) and Hoechst 33342 (blue). Scale bar, 5 μm (data representative of a minimum 10 images from 2 independent experiments). **e**, Quantification of confocal imaging as shown in **d** (each data point represents the average per cell per image; LipidTOX $P=0.0018$; lipid droplet no. $P<0.0001$). **f**, Quantification of triglyceride (TAG) levels from $\gamma\delta^{17}$ and $\gamma\delta^{\text{IFN}}$ cells expanded in vitro ($n=7$, each symbol represents one biological replicate). **g**, Filipin III staining of $\gamma\delta^{17}$ and $\gamma\delta^{\text{IFN}}$ cells ex vivo from LNs ($n=6$, data pooled from 2 independent experiments; $P=0.0276$). **h**, Bodipy-FL- C_{16} uptake in $\gamma\delta^{17}$ and $\gamma\delta^{\text{IFN}}$ cells from LNs ex vivo ($n=8$, data pooled from 2 independent experiments). **i**, Representative plots of Bodipy-FL- C_{16} uptake and IL-17 or IFN- γ production by $\gamma\delta^{17}$ and $\gamma\delta^{\text{IFN}}$ cells from LNs stimulated with PMA/ionomycin. **j**, Bodipy-FL- C_{16} MFI in IFN- γ ⁺ and IL-17⁺ $\gamma\delta$ T cells ($n=4$, data representative of 3 independent experiments). **k**, Representative plot of V γ 1 and V γ 4 expression in total $\gamma\delta$ T cells and percentage Bodipy-FL- C_{16} uptake by LN $\gamma\delta$ T cell subsets (V γ 1⁺, V γ 4⁺, V γ 1⁻4⁻) ($n=6$, data pooled from 2 independent experiments; V γ 1 versus V γ 4/V γ 6 $P<0.0001$; V γ 4 versus V γ 6 $P=0.0143$). **l**, Representative IFN- γ and IL-17 production by V γ 4⁺ $\gamma\delta$ T cells from LNs and percentage Bodipy-FL- C_{16} uptake by V γ 4⁺IFN- γ ⁺ and V γ 4⁺IL-17⁺ $\gamma\delta$ cells ($n=6$, data pooled from 2 independent experiments). **m**, Percentage Bodipy CholEsteryl FL- C_{12} uptake by $\gamma\delta^{17}$ (CD27⁻) and $\gamma\delta^{\text{IFN}}$ (CD27⁺) cells from LNs ex vivo ($n=6$, data pooled from 2 independent experiments). Error bars show mean \pm s.d., * $P<0.05$, ** $P<0.01$, *** $P<0.001$, **** $P<0.0001$ using unpaired two-tailed Student's *t*-test.

peutic performance of $\gamma\delta$ T cells in the clinic⁴⁴ is likely to require a better understanding of the factors that control the balance between $\gamma\delta^{17}$ and $\gamma\delta^{IFN}$ cell subsets in the TME.

Here, we also identified lipids as key $\gamma\delta^{17}$ -promoting factors, which is particularly relevant because tumors are known to be lipid-rich microenvironments^{4,5}. Palmitate and cholesterol ester



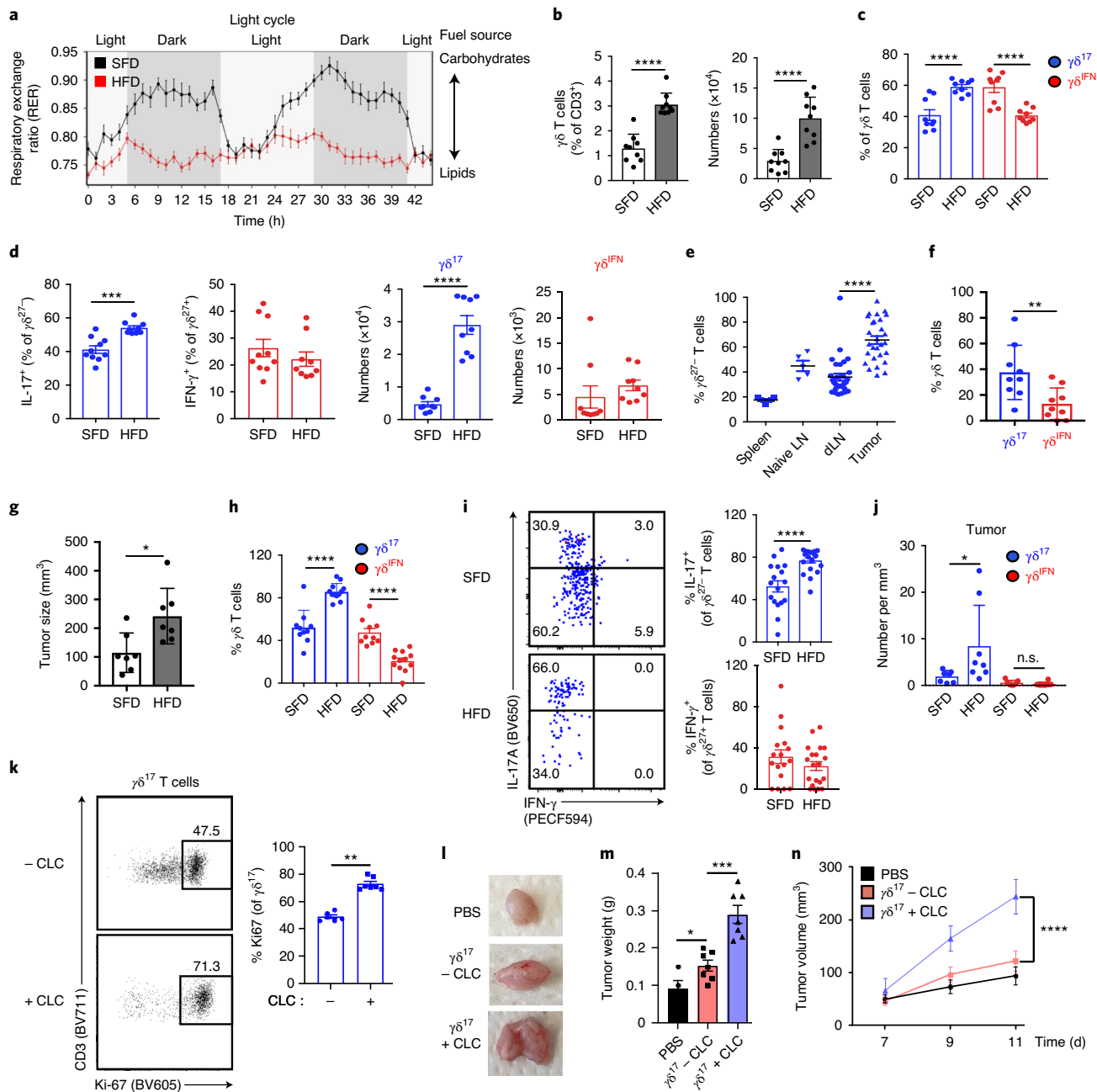


Fig. 6 | HFD promotes the expansion of pro-tumoral $\gamma\delta^{17}$ cells in lymph nodes and within tumors. **a**, RER of mice fed SFD or HFD for 8 weeks ($n=3$, data from 1 experiment). **b**, Bar graphs showing the percentage and absolute numbers of CD3⁺ $\gamma\delta$ T cells from LNs of SFD and HFD mice ($n=9$, data pooled from 3 independent experiments). **c**, Proportion of $\gamma\delta^{17}$ (CD27⁻) and $\gamma\delta^{IFN}$ (CD27⁺) cells in LNs of SFD and HFD fed mice ($n=9$, data pooled from 3 independent experiments). **d**, Percentage and absolute numbers of CD27⁺IFN- γ ⁺ and CD27⁻IL-17⁺ $\gamma\delta$ T cells from LNs of SFD and HFD mice ($n=9$, data pooled from 3 independent experiments). **e**, Proportion of infiltrating $\gamma\delta^{17}$ cells in spleen, draining LN and tumor in the B16 tumor model (dLN and tumor $n=30$, data pooled from 4 independent experiments; spleen $n=7$; naive LN $n=5$). **f**, Bar graph showing the percentage of $\gamma\delta^{17}$ and $\gamma\delta^{IFN}$ cells infiltrating tumors ($n=9$, data pooled from 2 experiments). **g**, Bar graph showing the size of tumors (mm³) in SFD and HFD fed mice. ($n=7$, representative of 3 independent experiments). **h**, Bar graph showing proportion of infiltrating $\gamma\delta^{17}$ (CD27⁻) and $\gamma\delta^{IFN}$ (CD27⁺) cells in tumors of SFD- and HFD-fed mice (SFD $n=10$, HFD $n=12$, data pooled from 2 independent experiments). **i**, Representative plots of IL-17 and IFN- γ expression in $\gamma\delta$ T cells infiltrating tumors of SFD- and HFD-fed mice. Bar graphs represent the percentage of $\gamma\delta^{17}$ and $\gamma\delta^{IFN}$ cells infiltrating tumors (SFD $n=17$, HFD $n=20$, data pooled from 3 independent experiments). **j**, Bar graph showing the number per mm³ of $\gamma\delta^{17}$ and $\gamma\delta^{IFN}$ cells in tumors of mice on SFD or HFD (SFD $n=7$, HFD $n=8$, data pooled from 2 independent experiments). **k**, Plots of proliferating Ki67⁺ $\gamma\delta^{17}$ cells cultured for 5h with or without cholesterol-loaded cyclodextrin (CLC). Graph represents the percentage of Ki67⁺ $\gamma\delta^{17}$ cells (data are representative of two independent experiments; pool of 3–5 mice per experiment). **l**, $\gamma\delta^{17}$ cells cultured (or not) with CLC for 5h were injected subcutaneously into E0771 tumors at day 7 and day 9 after tumor cell injection. Representative picture of tumors observed at day 11 post-E0771 cell inoculation. **m**, Graph showing tumor weight at day 11 following E0771 inoculation. CTRL versus $\gamma\delta^{17}$ - CLC ($P=0.0361$); $\gamma\delta^{17}$ - CLC versus $\gamma\delta^{17}$ + CLC ($P=0.0003$). **n**, E0771 tumor growth was monitored every 2 d after inoculation. Data in **l–n** are representative of 3 independent experiments ($n=3$ mice per experiment); $P < 0.0001$. Error bars show mean \pm s.d., * $P < 0.05$, ** $P < 0.01$, *** $P < 0.001$, **** $P < 0.0001$ using unpaired two-tailed Student's *t*-test or one-way ANOVA test with Šidák's post-hoc analysis.

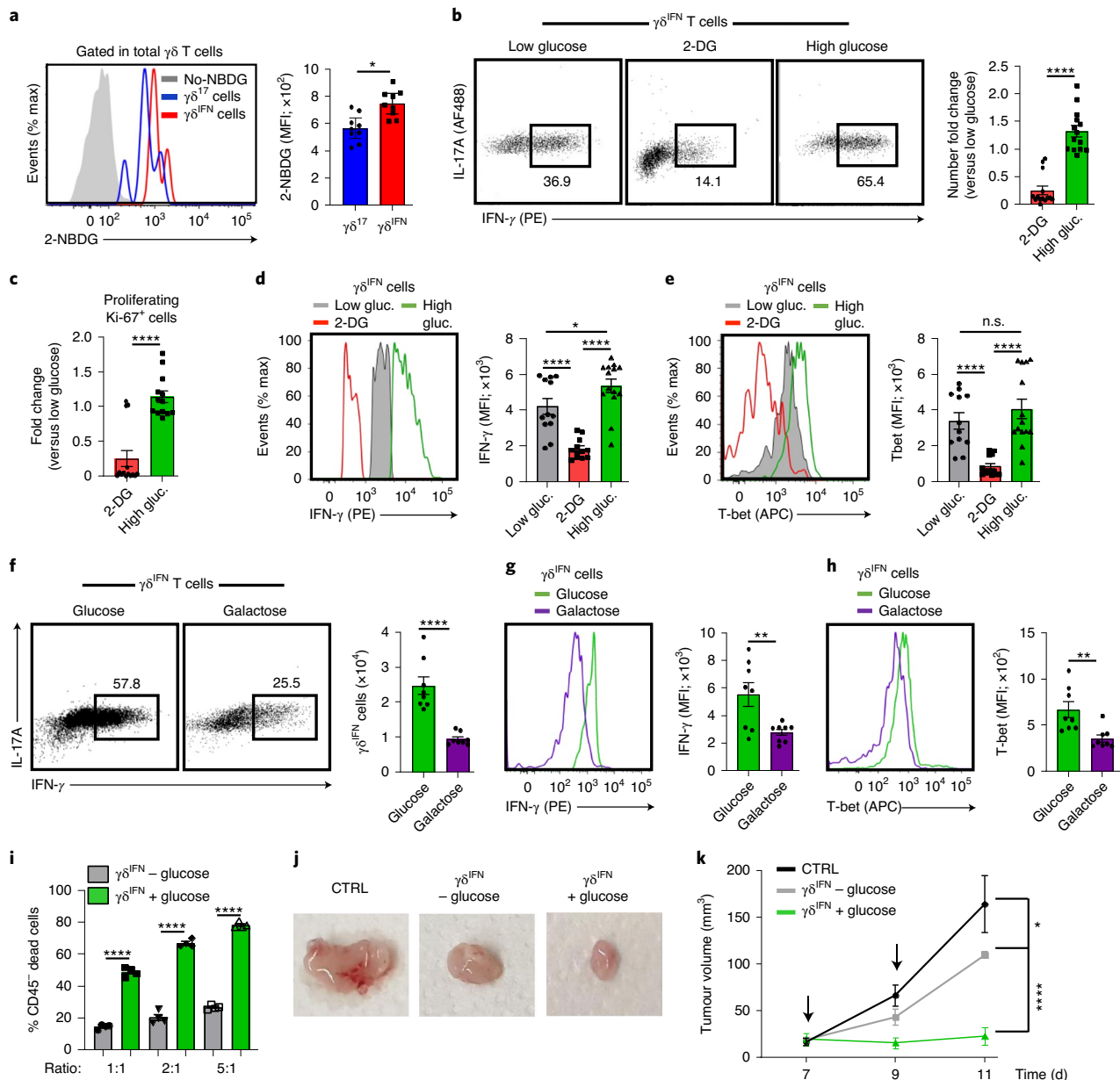


Fig. 7 | Glucose supplementation enhances the antitumor effector functions of $\gamma\delta^{IFN}$ cells. **a**, Glucose uptake assessed upon intravenous injection of fluorescent 2-NBDG in tumor-bearing mice. Tumors were collected 15 min later for analysis. Histogram represents 2-NBDG uptake in $\gamma\delta^{17}$ and $\gamma\delta^{IFN}$ cells ($P=0.047$). Data are representative of 2 independent experiments ($n=4$ mice per group and per experiment). **b–i**, Purified splenic and peripheral lymph node $\gamma\delta^{IFN}$ cells ($CD3^+TCR\gamma\delta^+CD27^+$) were cultured in the presence of IL-7 with medium containing low glucose (5 mM), 2-DG, high glucose (50 mM) or galactose (20 mM) for 78 h. **b**, Plots of peripheral $\gamma\delta^{IFN}$ cells cultured with IL-7 and medium containing low glucose, 2-DG or high glucose. Histogram represents the fold change in number of $\gamma\delta^{IFN}$ cells cultured with 2-DG or high glucose versus low glucose ($P<0.0001$). **c**, Fold change in number of proliferating Ki67⁺ $\gamma\delta^{IFN}$ cells cultured with 2-DG or high glucose versus low glucose ($P<0.0001$). **d**, IFN- γ expression was analyzed by flow cytometry in $\gamma\delta^{IFN}$ cells incubated with medium containing low glucose, 2-DG or high glucose. Histograms show the MFI of IFN- γ . Low glucose vs 2-DG ($P<0.0001$); 2-DG versus high glucose ($P<0.0001$); low glucose versus high glucose ($P=0.0115$). **e**, T-bet expression was analyzed by flow cytometry in $\gamma\delta^{IFN}$ cells incubated with medium containing low glucose, 2-DG or high glucose. Histograms show the MFI of T-bet. Low glucose vs 2-DG ($P<0.0001$); 2-DG versus high glucose ($P<0.0001$). **f**, Flow cytometry profiles of peripheral $\gamma\delta^{IFN}$ cells cultured with IL-7 and medium containing glucose (50 mM) or galactose (20 mM). Histogram represents the numbers of $\gamma\delta^{IFN}$ cells ($P<0.0001$). **g**, IFN- γ (**g**) and T-bet (**h**) expression was analyzed by flow cytometry in $\gamma\delta^{IFN}$ cells incubated with medium containing glucose or galactose ($P=0.0085$ for IFN- γ expression and $P=0.0034$ for T-bet expression). Histograms show the MFI of IFN- γ and T-bet. **i**, Summary of in vitro killing assay of E0771 tumor cells by $\gamma\delta^{IFN}$ cells previously supplemented (or not) with glucose (5 h preincubation); $P<0.0001$. Data are representative of 2 independent experiments ($n=3$ mice per group and per experiment). **j**, Representative picture of tumors observed at day 11 following E0771 inoculation. $\gamma\delta^{IFN}$ cells supplemented (or not) with glucose for 5 h were injected into the tumor at day 7 and day 9 after tumor cell injection. **k**, The E0771 tumor growth was monitored every 2 d for 11 d after E0771 inoculation. CTRL versus $\gamma\delta^{IFN}$ - glucose ($P=0.0148$); $\gamma\delta^{IFN}$ - glucose versus $\gamma\delta^{IFN}$ + glucose ($P<0.0001$). **b–e**, Data are representative of 4 independent experiments ($n=3$ mice per group and per experiment); **f–h**, data are representative of 2 independent experiments ($n=4$ mice per group and per experiment); **j**, **k**, data are representative of 2 independent experiments ($n=5$ mice per group and per experiment). Error bars show mean \pm s.e.m., * $P<0.05$, ** $P<0.01$, **** $P<0.0001$ using unpaired two-tailed Student's *t*-test or ANOVA test.

uptake were higher in $\gamma\delta^{17}$ than in $\gamma\delta^{\text{IFN}}$ cells. Thus, we propose that the increase in intracellular lipids is due to enhanced uptake, although endogenous lipid synthesis cannot be ruled out. Our findings that $\gamma\delta^{17}$ cell proliferation is boosted by cholesterol treatment, and that these cells expand substantially in obese mice, provide additional evidence that HFD causes a systemic increase in the $\gamma\delta^{17}$ subset, consistent with previous findings in the skin⁴⁵ and lungs⁴⁶, and may provide a mechanistic understanding for this expansion. Obesity is a known risk factor for cancer, and we have previously demonstrated the link between obesity and suppression of natural killer (NK) cell antitumor function⁴⁷. Given that $\gamma\delta^{17}$ cells have strong protumoral effects and we find this population to be expanded in tumors of obese mice, this may represent an additional mechanism linking cancer and obesity, whereby abundant lipids favor $\gamma\delta^{17}$ over $\gamma\delta^{\text{IFN}}$ cells to support tumor growth.

Conversely, we found $\gamma\delta^{\text{IFN}}$ cells, from their thymic development to intratumoral functions, to be boosted by glucose metabolism. Naturally, the large consumption of glucose by tumor cells⁷ creates a major metabolic constraint on $\gamma\delta^{\text{IFN}}$ TILs. Glucose restriction can impair T cell cytokine production^{5,6}, while production of lactate by tumor cells performing aerobic glycolysis can inhibit T cell proliferation and cytotoxic functions⁴⁸. Therefore, we do not conceive glucose supplementation as an appropriate strategy to enhance endogenous T cell (including $\gamma\delta^{\text{IFN}}$) responses in vivo. Instead, we suggest that it should be considered in protocols used to expand/differentiate $\gamma\delta$ T cells ex vivo for adoptive cell therapy. Such an 'in vitro glucose boost' may enable stronger antitumor activities (namely, IFN- γ production and cytotoxicity) upon T cell transfer, as suggested by our data using CD27⁺ $\gamma\delta^{\text{IFN}}$ cells in the breast cancer model, although evaluation of the duration and long-term impact of this 'boost' requires further investigation in slower growing tumor models.

While we did not dissect the mechanistic link between aerobic glycolysis and IFN- γ production by CD27⁺ $\gamma\delta^{\text{IFN}}$ cells, previous studies on $\alpha\beta$ T cells have shown that glycolysis controls (via the enzyme GAPDH) the translation of IFN- γ mRNA⁵. Moreover, glycolysis was shown to be essential for the cytotoxic activity of NK cells, namely their degranulation and Fas ligand expression, upon engagement of NK cell receptors (NKR)s⁴⁹. This is particularly interesting when considering the potential of a human $\gamma\delta$ T cell product that we developed for adoptive cell therapy of cancer, Delta One T (DOT) cells. These human V δ 1⁺ T cells are induced in vitro to express high levels of NKR that enhance their cytotoxicity and IFN- γ production^{9,50}. We therefore propose high-dose glucose to be added to the DOT protocol as to further increase their antitumor potential.

In sum, this study demonstrates that thymic differentiation of effector $\gamma\delta$ T cell subsets, besides well-established epigenetic and transcriptional regulation, includes divergent metabolic programming that is sustained in the periphery and, in particular, in the TME. It further identifies distinct metabolic resources that control the intratumoral activities of $\gamma\delta$ T cell subsets, with lipids favoring $\gamma\delta^{17}$ cells and glucose enhancing $\gamma\delta^{\text{IFN}}$ cells, which provides a new metabolism-based angle for therapeutic intervention in cancer and possibly other diseases.

Online content

Any methods, additional references, Nature Research reporting summaries, source data, extended data, supplementary information, acknowledgements, peer review information; details of author contributions and competing interests; and statements of data and code availability are available at <https://doi.org/10.1038/s41590-020-00848-3>.

Received: 27 April 2020; Accepted: 24 November 2020;
Published online: 18 January 2021

References

- Buck, M. D., Sowell, R. T., Kaech, S. M. & Pearce, E. L. Metabolic instruction of immunity. *Cell* **169**, 570–586 (2017).
- Almeida, L., Lochner, M., Berod, L. & Sparwasser, T. Metabolic pathways in T cell activation and lineage differentiation. *Semin. Immunol.* **28**, 514–524 (2016).
- Geltink, R. I. K., Kyle, R. L. & Pearce, E. L. Unraveling the complex interplay between T cell metabolism and function. *Annu. Rev. Immunol.* **36**, 461–488 (2018).
- Cham, C. M., Driessens, G., O'Keefe, J. P. & Gajewski, T. F. Glucose deprivation inhibits multiple key gene expression events and effector functions in CD8⁺ T cells. *Eur. J. Immunol.* **38**, 2438–2450 (2008).
- Chang, C. H. et al. Posttranscriptional control of T cell effector function by aerobic glycolysis. *Cell* **153**, 1239–1251 (2013).
- Chang, C. H. et al. Metabolic competition in the tumor microenvironment is a driver of cancer progression. *Cell* **162**, 1229–1241 (2015).
- O'Sullivan, D., Sanin, D. E., Pearce, E. J. & Pearce, E. L. Metabolic interventions in the immune response to cancer. *Nat. Rev. Immunol.* **19**, 324–335 (2019).
- Silva-Santos, B., Mensurado, S. & Coffelt, S. B. $\gamma\delta$ T cells: pleiotropic immune effectors with therapeutic potential in cancer. *Nat. Rev. Cancer* **19**, 392–404 (2019).
- Sebestyén, Z., Prinz, I., Déchanet-Merville, J., Silva-Santos, B. & Kuball, J. Translating gammadelta ($\gamma\delta$) T cells and their receptors into cancer cell therapies. *Nat. Rev. Drug Discov.* **19**, 169–184 (2020).
- Chien, Y. H., Meyer, C. & Bonneville, M. $\gamma\delta$ T cells: first line of defense and beyond. *Annu. Rev. Immunol.* **32**, 121–155 (2014).
- Hayday, A. C. $\gamma\delta$ T cells and the lymphoid stress-surveillance response. *Immunity* **31**, 184–196 (2009).
- Hayday, A. C. $\gamma\delta$ T cell update: adaptate orchestrators of immune surveillance. *J. Immunol.* **203**, 311–320 (2019).
- Ravens, S. et al. Human $\gamma\delta$ T cells are quickly reconstituted after stem-cell transplantation and show adaptive clonal expansion in response to viral infection. *Nat. Immunol.* **18**, 393–401 (2017).
- Kohlgruber, A. C. et al. $\gamma\delta$ T cells producing interleukin-17A regulate adipose regulatory T cell homeostasis and thermogenesis. *Nat. Immunol.* **19**, 464–474 (2018).
- Ribeiro, M. et al. Meningeal $\gamma\delta$ T cell-derived IL-17 controls synaptic plasticity and short-term memory. *Sci. Immunol.* <https://doi.org/10.1126/sciimmunol.aay5199> (2019).
- Papotto, P. H., Ribot, J. C. & Silva-Santos, B. IL-17⁺ $\gamma\delta$ T cells as kick-starters of inflammation. *Nat. Immunol.* **18**, 604–611 (2017).
- Jensen, K. D. et al. Thymic selection determines $\gamma\delta$ T cell effector fate: antigen-naïve cells make interleukin-17 and antigen-experienced cells make interferon γ . *Immunity* **29**, 90–100 (2008).
- Ribot, J. C. et al. CD27 is a thymic determinant of the balance between interferon- γ - and interleukin 17-producing $\gamma\delta$ T cell subsets. *Nat. Immunol.* **10**, 427–436 (2009).
- Sumaria, N., Grandjean, C. L., Silva-Santos, B. & Pennington, D. J. Strong TCR $\gamma\delta$ signaling prohibits thymic development of IL-17A-secreting $\gamma\delta$ T cells. *Cell Rep.* **19**, 2469–2476 (2017).
- Muñoz-Ruiz, M. et al. TCR signal strength controls thymic differentiation of discrete proinflammatory $\gamma\delta$ T cell subsets. *Nat. Immunol.* **17**, 721–727 (2016).
- Muñoz-Ruiz, M., Sumaria, N., Pennington, D. J. & Silva-Santos, B. Thymic determinants of $\gamma\delta$ T cell differentiation. *Trends Immunol.* **38**, 336–344 (2017).
- Silva-Santos, B., Serre, K. & Norell, H. $\gamma\delta$ T cells in cancer. *Nat. Rev. Immunol.* **15**, 683–691 (2015).
- Argüello, R. J. et al. SCENITH: a flow cytometry based method for functional profiling energy metabolism with single cell resolution. *Cell Metab.* **32**, 1063–1075.e7 (2020).
- Gleyzer, N., Vercauteren, K. & Scarpulla, R. C. Control of mitochondrial transcription specificity factors (TFB1M and TFB2M) by nuclear respiratory factors (NRF-1 and NRF-2) and PGC-1 family coactivators. *Mol. Cell. Biol.* **25**, 1354–1366 (2005).
- Scarpulla, R. C. Nuclear control of respiratory chain expression in mammalian cells. *J. Bioenerg. Biomembr.* **29**, 109–119 (1997).
- Dang, C. V. et al. The c-Myc target gene network. *Semin. Cancer Biol.* **16**, 253–264 (2006).
- Guo, Q. M. et al. Identification of c-myc responsive genes using rat cDNA microarray. *Cancer Res.* **60**, 5922–5928 (2000).
- In, T. S. H. et al. HEB is required for the specification of fetal IL-17-producing $\gamma\delta$ T cells. *Nat. Commun.* **8**, 2004 (2017).
- Coffey, F. et al. The TCR ligand-inducible expression of CD73 marks $\gamma\delta$ lineage commitment and a metastable intermediate in effector specification. *J. Exp. Med.* **211**, 329–343 (2014).
- Turchinovich, G. & Hayday, A. C. Skint-1 identifies a common molecular mechanism for the development of interferon- γ -secreting versus interleukin-17-secreting $\gamma\delta$ T cells. *Immunity* **35**, 59–68 (2011).

31. Lu, Y., Cao, X., Zhang, X. & Kovalovsky, D. PLZF controls the development of fetal-derived IL-17⁺V γ 6⁺ $\gamma\delta$ T cells. *J. Immunol.* **195**, 4273–4281 (2015).
32. Tan, L. et al. Single-cell transcriptomics identifies the adaptation Scart1⁺ V γ 6⁺ T cells to skin residency as activated effector cells. *Cell Rep.* **27**, 3657–3671.e4 (2019).
33. McCully, M. L. et al. Skin metabolites define a new paradigm in the localization of skin tropic memory T cells. *J. Immunol.* **195**, 96–104 (2015).
34. Bartz, R. et al. Lipidomics reveals that adiposomes store ether lipids and mediate phospholipid traffic. *J. Lipid Res.* **48**, 837–847 (2007).
35. Le Goffe, C., Vallette, G., Jarry, A., Bou-Hanna, C. & Laboisse, C. L. The in vitro manipulation of carbohydrate metabolism: a new strategy for deciphering the cellular defence mechanisms against nitric oxide attack. *Biochem. J.* **344**, 643–648 (1999).
36. Bustamante, E. & Pedersen, P. L. High aerobic glycolysis of rat hepatoma cells in culture: role of mitochondrial hexokinase. *Proc. Natl Acad. Sci. USA* **74**, 3735–3739 (1977).
37. Buck, M. D., O'Sullivan, D. & Pearce, E. L. T cell metabolism drives immunity. *J. Exp. Med.* **212**, 1345–1360 (2015).
38. Menk, A. V. et al. Early TCR signaling induces rapid aerobic glycolysis enabling distinct acute T cell effector functions. *Cell Rep.* **22**, 1509–1521 (2018).
39. Shin, B. et al. Mitochondrial oxidative phosphorylation regulates the fate decision between pathogenic T_H17 and regulatory T cells. *Cell Rep.* **30**, 1898–1909.e4 (2020).
40. Di Luccia, B., Gilfillan, S., Cella, M., Colonna, M. & Huang, S. C. ILC3s integrate glycolysis and mitochondrial production of reactive oxygen species to fulfill activation demands. *J. Exp. Med.* **216**, 2231–2241 (2019).
41. Schmolka, N. et al. Epigenetic and transcriptional signatures of stable versus plastic differentiation of proinflammatory $\gamma\delta$ T cell subsets. *Nat. Immunol.* **14**, 1093–1100 (2013).
42. Schmolka, N., Wencker, M., Hayday, A. C. & Silva-Santos, B. Epigenetic and transcriptional regulation of $\gamma\delta$ T cell differentiation: programming cells for responses in time and space. *Semin. Immunol.* **27**, 19–25 (2015).
43. Gentles, A. J. et al. The prognostic landscape of genes and infiltrating immune cells across human cancers. *Nat. Med.* **21**, 938–945 (2015).
44. Legut, M., Cole, D. K. & Sewell, A. K. The promise of $\gamma\delta$ T cells and the $\gamma\delta$ T cell receptor for cancer immunotherapy. *Cell Mol. Immunol.* **12**, 656–668 (2015).
45. Nakamizo, S. et al. High fat diet exacerbates murine psoriatic dermatitis by increasing the number of IL-17-producing $\gamma\delta$ T cells. *Sci. Rep.* **7**, 14076 (2017).
46. Goldberg, E. L. et al. Ketogenic diet activates protective $\gamma\delta$ T cell responses against influenza virus infection. *Sci. Immunol.* <https://doi.org/10.1126/sciimmunol.aav2026> (2019).
47. Michelet, X. et al. Metabolic reprogramming of natural killer cells in obesity limits antitumor responses. *Nat. Immunol.* **19**, 1330–1340 (2018).
48. Fischer, K. et al. Inhibitory effect of tumor cell-derived lactic acid on human T cells. *Blood* **109**, 3812–3819 (2007).
49. Wang, Z. et al. Glycolysis and oxidative phosphorylation play critical roles in natural killer cell receptor-mediated natural killer cell functions. *Front Immunol.* **11**, 202 (2020).
50. Almeida, A. R. et al. Delta one T cells for immunotherapy of chronic lymphocytic leukemia: clinical-grade expansion/differentiation and preclinical proof of concept. *Clin. Cancer Res.* **22**, 5795–5804 (2016).

Publisher's note Springer Nature remains neutral with regard to jurisdictional claims in published maps and institutional affiliations.

© The Author(s), under exclusive licence to Springer Nature America, Inc. 2021

Methods

Ethics statement. All mouse experiments performed in this study were evaluated and approved by the Instituto de Medicina Molecular Orbea institutional ethical committee and the DGAV national competent authority under the license number 019069, the UK Home Office regulations and institutional guidelines under license number 70/8758, the Institutional Animal Care and Use Committee of Brigham and Women's Hospital and Harvard Medical School and the Trinity College Dublin ethics committee. Euthanasia was performed by CO₂ inhalation. Anesthesia was performed by isoflurane inhalation.

Mice and tumor cell lines. C57Bl/6J (B6) WT mice and Myc-GFP mice (B6;129-Myc^{tm1Slck⁺}) were purchased from Charles River and Jackson Laboratories. PLZF-GFP (*Zbtb16^{GFP}*) mice were generated in the laboratory of D. Sant'Angelo as described previously⁵¹. Mice were maintained under specific pathogen-free conditions. Standard food and water were given ad libitum. Where indicated, mice were fed a HFD (Research Diets; D12492) for 8 weeks. Mice were used at the fetal (embryonic day 14–18), neonatal (1–5 d old) or adult (6–12 weeks old) stages.

The E0771 murine breast adenocarcinoma cells, MC38 murine colon adenocarcinoma cells and B16.F10 melanoma cells were purchased from ATCC. Cells were maintained in DMEM with 10% (vol/vol) FCS (Gibco; Thermo Fisher Scientific) and 1% (vol/vol) penicillin–streptomycin (Sigma-Aldrich).

Tumor transplantation in vivo. Mice were injected with 1×10^6 E0771 tumor cells in fat pads, 1×10^6 MC38 tumor cells or 2×10^5 cells B16 tumor cells subcutaneously into the right shaved flank. Tumor growth was measured every 2–3 d using calipers, and animals were euthanized when tumors reached a diameter (*D*) of 15 mm; when tumors became ulcerous; or 1 or 2 weeks after tumor injection. Tumor size was calculated using the following formula: $(D_1)^2 \times (D_2 / 2)$, *D*₁ being the smaller value of the tumor diameter. In some experiments, mice were fed a HFD (60% calories from lard) for 10 weeks prior to tumor injection, and the HFD was continued throughout the experiment.

Comprehensive lab-animal monitoring system. Indirect calorimetry data were recorded using a Promethion Metabolic Cage System (Sable Systems) essentially as described previously⁵². Mice were housed individually in metabolic chambers under a 12-h light–dark cycle at room temperature (22 °C) with free access to food and water. Mice were acclimated for 24 h in metabolic cages before recording calorimetric variables. Mice were fed either a standard chow diet or a high fat (60%) diet ad libitum for 8 weeks prior to being placed in metabolic cages and were maintained on either diet throughout the recording.

Tissue processing and cell isolation. Tumors were collected and digested with 1 mg ml⁻¹ collagenase type I, 0.4 mg ml⁻¹ collagenase type IV (Worthington) and 10 µg ml⁻¹ DNase I (Sigma-Aldrich) for 30 min at 37 °C. Cell suspensions were then filtered through a 100-µm nylon cell strainer (Falcon/Corning). γδ T cells were isolated by scratching thymus, spleen and lymph node on a 70-µm mesh. Lungs were minced then homogenized in RPMI-1640 using a TissueLyser (Qiagen) and filtered through a 70-µm mesh. Adipose tissue was processed as described previously⁵³. Red blood cells were lysed using RBC Lysis Buffer (Biolegend) or ammonium chloride lysis buffer (made in-house). Single-cell suspensions of fetal and neonatal thymocytes were obtained by gently homogenizing thymic lobes followed by straining through 40-µm strainers (BD).

For cell sorting, γδ T cells were pre-enriched by depletion of CD4⁺ and CD8⁺ T cells, dendritic cells and B cells using biotinylated anti-CD4 (RM4-5), anti-CD8 (53-6.7), anti-CD11c (N14) and anti-CD19 (6D5) antibodies with anti-biotin microbeads (Miltenyi Biotec) by QuadroMACS or γδ T cells were purified using TCRγ/δ T Cell Isolation Kit, mouse (Miltenyi Biotec). Cells were sorted on a FACS Aria III (BD Biosciences).

Cell culture. CD27⁻ γδ T cells were expanded in vitro as previously described⁵⁴. This protocol was adapted to expand CD27⁺ γδ T cells by using 10 ng ml⁻¹ IL-2, 10 ng ml⁻¹ IL-15 and 20 ng ml⁻¹ IL-7. For downstream assays, γδ T cells were purified using TCRγ/δ T Cell Isolation Kit, mouse (Miltenyi Biotec). Ex vivo cultures were performed using RPMI-1640 (Gibco) supplemented with 10% heat-inactivated fetal bovine serum (Gibco), 1% penicillin–streptomycin, 1% L-glutamine. For cytokine stimulation, cells were cultured with 10 ng ml⁻¹ IL-1β and IL-23 (Miltenyi Biotec) and/or IL-12 and IL-18 (BioLegend).

For short-term skin-draining-lymphocyte cultures, single-cell suspensions of lymphocytes were isolated from skin-draining lymph nodes from adult B6 mice. Cells were resuspended in complete RPMI medium (RPMI-1640 with 10% FCS, 1% penicillin and streptomycin, and 2 mM L-glutamine). Then, 1×10^6 lymphocytes in 500 µl of complete medium were incubated for 48 h in 48-well plates either under control conditions or with the addition of 5-aminoimidazole-4-carboxamide (AICAR; 1.6 mM; Sigma-Aldrich). Cells were subsequently analyzed by flow cytometry.

Fetal thymic organ cultures. E15–E17 thymic lobes from B6 mice were cultured on nucleopore membrane filter disks (Whatman) in FTOC medium (RPMI-1640 with 10% FCS, 1% penicillin–streptomycin, 50 µM β-mercaptoethanol (Invitrogen) and 2 mM L-glutamine (Sigma-Aldrich)) for 6–12 d (unless otherwise indicated). In some experiments, 2-deoxyglucose (2-DG; 0.6 mM), fasentin (0.6 mM), metformin (2 mM) or oligomycin (1 nM) were added to the cultures. All thymic organ cultures were subsequently analyzed by flow cytometry. In some cultures, where concentration of glucose was manipulated, 'basic' FTOC medium (RPMI-1640 – glucose with 10% FCS, 1% penicillin–streptomycin, 50 µM β-mercaptoethanol (Invitrogen) and 2 mM L-glutamine (Sigma-Aldrich)) was used, and glucose was added at 5 mM for 'low-glucose' conditions or 25 mM for 'high-glucose' conditions.

In some experiments, anti-TCRδ antibody (GL3; 1 µg ml⁻¹ unless otherwise indicated) was added to the cultures. Cultures containing antibodies were rested overnight in fresh FTOC medium before analysis. All thymic organ cultures were subsequently analyzed by flow cytometry.

Manipulation of γδ metabolic pathways in vitro and in vivo. Spleen and lymph nodes were collected from C57Bl/6J mice. Cell suspensions were stained with LIVE/DEAD Fixable Near-IR (Thermo Fisher Scientific), anti-CD3e (145-2C11), anti-TCRδ (GL3) and anti-CD27 (LG.7F9) for 15 min at 4 °C. CD27⁺ and CD27⁻ γδ T cells were sorted by FACS. CD27⁺ and CD27⁻ γδ T cells were incubated on plate-bound anti-CD3e (145-2C11) (10 µg ml⁻¹) in the presence of IL-7 (50 µg ml⁻¹) or IL-7 (50 µg ml⁻¹), IL-1β (10 µg ml⁻¹) and IL-23 (10 µg ml⁻¹), respectively. All cytokines were purchased from Peprotech. Then, cells were cultured with 2-deoxy-D-glucose (2-DG; 2 mM; Sigma-Aldrich), high D-glucose (50 mM; Sigma-Aldrich), galactose (20 mM; Sigma-Aldrich), carbonyl cyanide-4-(trifluoromethoxy) phenylhydrazone (FCCP; 1 µM; Sigma-Aldrich) and cholesterol-loaded cyclodextrin (CLC; 5 µg ml⁻¹) for 5 h at 37 °C for in vitro experiments.

For experiments in vivo, purified CD27⁻ and CD27⁺ γδ T cells were incubated (or not) for 5 h with cholesterol-loaded cyclodextrin (5 µg ml⁻¹) or with high D-glucose (50 mM; Sigma-Aldrich), respectively; 5×10^5 CD27⁻ or 1×10^6 CD27⁺ γδ T cells were injected twice directly at the tumor site (first injection 7 d after tumor inoculation and second injection 2 d later). Mice were analyzed 11 d after tumor cell injection.

For lipid depletion in vivo, mice were injected daily with 50 mg kg (body weight) orlistat i.p. on days 6–9 after tumor injection, then tumor cell infiltrate was analyzed on day 10.

In vitro killing assays. Purified CD27⁺ γδ T cells were supplemented (or not) with high levels of glucose (50 mM; Sigma-Aldrich) for 5 h at 37 °C, 5% CO₂. Then, variable numbers of CD27⁺ γδ T cells were cocultured with 5×10^5 E0771 breast cancer cells in complete RPMI Medium (minus D-glucose). The killing capacities of CD27⁺ γδ T cells based on death of E0771 cells (Annexin V staining) were assessed by flow cytometry after 24 h.

Flow cytometry. γδ T cells were analyzed by flow cytometry using standard procedures. For surface staining, cells were Fc-blocked with anti-CD16/32 (clone 93; eBioscience) and incubated for 15 min at 4 °C with antibodies and LIVE/DEAD Fixable Near-IR (Thermo Fisher Scientific) or viability dye Zombie NIR stain (BioLegend) in FACS buffer (PBS 1×, 2% FCS, 1 mM EDTA). Anti-CD3e (145-2C11; 1:400), anti-CD27 (LG.7F9; 1:200), anti-CD25 (PC61; 1:400), anti-CD73 (TY/11.8; 1:200) and anti-Vγ2 (UC3-10A6; 1:200) were purchased from eBioscience. Anti-CD45 (30-F11; 1:400), anti-TCRδ (GL3; 1:200), anti-CD24 (M1/69; 1:400), anti-Vγ1 (2.11; 1:100), anti-Vγ4 (UC3-10A6; 1:200), anti-Vγ5 (536; 1:200) and anti-CD45RB (C363-16A; 1:400) were purchased from BioLegend and anti-CD44 (IM7; 1:400) from BD Pharmingen. Cells were washed with FACS buffer. For intracellular cytokine staining, cells were stimulated with 50 µg ml⁻¹ phorbol 12-myristate 13-acetate (PMA; Sigma-Aldrich) and 1 µg ml⁻¹ ionomycin (Sigma-Aldrich) for 3–4 h at 37 °C, 5% CO₂ in the presence of 10 µg ml⁻¹ brefeldin-A (Sigma-Aldrich) and 2 µM monensin (eBioscience). Cells were fixed and permeabilized with Foxp3 staining kit (eBioscience/Thermo Fisher Scientific), according to the manufacturer's instructions. Cells were incubated for 30 min at 4 °C, with the following antibodies from eBioscience: anti-IFN-γ (XMG1.2; 1:100), Ki67 (SolA15; 1:800), T-bet (4B10; 1:150) and RORγt (B2D; 1:100). Anti-IL-17F (9D3.1C8; 1:100) and IL-17A (TC11-18H10.1; 1:100) were purchased from Biolegend. For Annexin V staining, the Annexin V Kit (eBioscience) was used following the manufacturer's instructions.

The following dyes were purchased from Invitrogen and stained according to manufacturer's instructions: MitoTracker Green FM, tetramethylrhodamine methyl ester perchlorate (TMRM), HCS LipidTOX Red Neutral Lipid Stain. Palmitate uptake was measured using 1 µM Bodipy-FL-C₁₆ (Invitrogen) incubated for 10 min at 37 °C. Cholesterol ester uptake was measured using 2 µM Bodipy CholEsteryl FL-C₁₂ incubated for 1 h at 37 °C. Cholesterol content was measured using 50 µg ml⁻¹ Filipin III (Sigma-Aldrich) incubated for 1 h at room temperature.

Flow cytometry analysis was performed with a FACS Fortessa, LSRII or Canto II using FACS Diva Software (BD Biosciences) and data were analyzed using FlowJo software (BD Biosciences).

Seahorse metabolic flux analysis. Real-time analysis of OCRs and ECARs of IFN- γ - and IL-17-committed $\gamma\delta$ T cells sorted from 5-d-old B6 pups and CD27^{+/+}- $\gamma\delta$ T cells from spleen/lymph nodes expanded in vitro were assessed using the XFp Extracellular Flux or Seahorse XFe-96 analyzers, respectively (Seahorse Bioscience). Cells were added to a Seahorse XFe96 Cell Culture Microplate (Agilent) and coated with Cell-Tak (Corning) to ensure adherence, and sequential measurements of ECAR and OCR were performed in XF RPMI Seahorse medium supplemented with glucose (10 mM), glutamine (2 mM) and sodium pyruvate (1 mM) following the addition of oligomycin A (2 μ M), FCCP (2 μ M), rotenone (1 μ M) plus antimycin A (1–4 μ M). Basal glycolysis, glycolytic capacity, basal mitochondrial respiration and maximal mitochondrial respiration were calculated. OCR and ECAR values were normalized to cell number.

SCENITH. Cells were plated at 20×10^6 cells ml⁻¹ in 96-well plates. After activation of $\gamma\delta$ T cells, cells were treated for 30 min at 37 °C, 5% CO₂ with control, 2-DG (100 mM; Sigma-Aldrich), oligomycin (1 μ M; Sigma-Aldrich) or a combination of both drugs. Puromycin (10 μ g ml⁻¹; Sigma-Aldrich) is added for 15 min at 37 °C. The SCENITH kit (<http://www.scenith.com>) containing all reagents and protocols was developed by R. Argüello (CIML). Cells were washed in cold PBS and stained with primary conjugated antibodies against different surface markers (as described above) for 15 min at 4 °C in FACS buffer (PBS 1 \times 5% FCS, 2 mM EDTA). After washing with FACS buffer, cells were fixed and permeabilized using Cytofix/Cytoperm (BD) following the manufacturer's instructions. Intracellular staining of puromycin using the anti-puro monoclonal antibody (1:600, Clone R4743L-E8) was performed by incubating cells during 30 min at 4 °C diluted in Permash. Experimental duplicates were performed in all conditions.

In vivo glucose uptake. 2-NBDG (300 μ g diluted in PBS 1 \times ; Cayman Chemical) was injected intravenously in C57Bl/6J mice; 15 min later, cells from tumors were collected.

Assessment of mitochondrial morphology. Mitochondrial membrane potential was measured using tetramethylrhodamine, ethyl ester (TMRE; 100 nM; Abcam) according to manufacturer protocols. Following TMRE staining, carbonyl cyanide-4-(trifluoromethoxy) phenylhydrazone (FCCP; 25 μ M; Abcam) was used as a positive control for mitochondrial membrane depolarization. Total mitochondrial mass was assessed using MitoTracker Green (Invitrogen) according to manufacturer's instructions. All cells were subsequently analyzed by flow cytometry.

Triglyceride quantification. Triglycerides (TAGs) were quantified from expanded $\gamma\delta$ T cells in vitro using Picoprobe Triglyceride Quantification Assay Kit, Fluorometric (Abcam) and absorbance measured using FLUOstar OPTIMA (BMG Labtech).

RNA isolation and real-time PCR. mRNA was prepared from FACS-sorted CD27⁺ and CD27⁻ $\gamma\delta$ T cells from WT spleen and draining lymph nodes using High Pure RNA Isolation kit (Roche). Reverse transcription was performed with random oligonucleotides (Invitrogen). Results were normalized to actin mRNA. qPCR was performed with SYBR Premix Ex Taq master mix (Takara) on an ABI ViiA7 cycler (Applied Biosystems). The CT for the target gene was subtracted from the CT for the endogenous reference, and the relative amount was calculated as $2^{-\Delta\Delta CT}$.

Imaging. Thymocytes from B6 E15 thymic lobes cultured for 12 d were isolated and stained for surface markers and then MitoTracker Green or TMRE (as described above). All cells were subsequently analyzed on an ImageStream Mark II imaging flow cytometer using INSPIRE acquisition software (Amnis); 30,000 events were saved from samples, and 1,000 positive events from compensation single color controls. Analysis was performed using IDEAS version 6.2.

For lipid droplet quantification, $\gamma\delta$ T cells expanded in vitro were stained with LipidTOX red neutral lipid stain (Invitrogen) and Hoechst 33342 (Sigma-Aldrich). MitoTracker Green FM (Invitrogen) was used to identify mitochondria. Cells were mounted onto poly-L-lysine coated slides. Images were obtained with a Zeiss LSM 800 confocal microscope using Zen 2.3 software (Zeiss) and analyzed using ImageJ.

RNA-seq and data processing. Single-cell sequencing libraries were generated using the Chromium Single Cell 5' Library and Gel Bead Kit (10X Genomics) according to the manufacturer's instructions. Data was analyzed using the R package Seurat v2.3 (refs. 55,56).

UMI counts were normalized using regularized negative binomial regression with the sctransform package⁵⁷. For downstream analysis of normalized data, principal component analysis (PCA) was performed using $n = 50$ dimensions, and PCA variability was determined using an Elbow plot. Differential gene expression analysis and GSEA was performed using the MAST and fgsea packages^{56,57}. Pathways and gene lists for gene set enrichment analysis were obtained using the msigdb package from Molecular Signatures database (MSigDB)^{58,59}. Adaptively

thresholded Low Rank Approximation (ALRA) from the Seurat wrappers package was performed to correct for drop-out values for visualization of leading-edge and differentially expressed genes identified by MAST⁶⁰.

All downstream analysis was performed using R v.3.6.3 and RStudio Desktop 1.2.5001 on an Ubuntu 19.10 linux (64-bit) system using the following R packages and libraries: dplyr v.0.8.5, fgsea v.1.12.0, ggplot2 v.3.3.0, MAST v.1.12.0, sctransform v.0.2.1, Seurat v.3.1.4, SeuratWrappers v.0.1.0, uwot v.0.1.8 and viridis v.0.5.1.

Statistical analysis. Statistical analysis was performed using GraphPad Prism software using non-parametric two-tailed Mann–Whitney test or, if both groups followed a normal distribution (tested by D'Agostino and Pearson normality test), using two-tailed unpaired Student's *t*-test or one-way ANOVA. All data are presented as means \pm standard error of mean s.e.m. or standard deviation s.d. **P* < 0.05; ***P* < 0.01; ****P* < 0.001, *****P* < 0.0001.

Reporting Summary. Further information on research design is available in the Nature Research Reporting Summary linked to this article.

Data availability

The GEO public repository accession codes are GSE150585 for single-cell RNA sequencing; and GSE156782 for bulk RNA sequencing. The data that support the findings of this study are available from the corresponding author upon request.

References

- Lynch, L. et al. Regulatory *i*NKT cells lack expression of the transcription factor PLZF and control the homeostasis of T_{reg} cells and macrophages in adipose tissue. *Nat. Immunol.* **16**, 85–95 (2015).
- Vu, J. P. et al. Long-term intake of a high-protein diet affects body phenotype, metabolism, and plasma hormones in mice. *J. Nutr.* **147**, 2243–2251 (2017).
- Kohlgruber, A. C. et al. $\gamma\delta$ T cells producing interleukin-17A regulate adipose regulatory T cell homeostasis and thermogenesis. *Nat. Immunol.* **19**, 464–474 (2018).
- McKenzie, D. R. et al. IL-17-producing $\gamma\delta$ T cells switch migratory patterns between resting and activated states. *Nat. Commun.* **8**, 15632 (2017).
- Butler, A., Hoffman, P., Smibert, P., Papalexis, E. & Satija, R. Integrating single-cell transcriptomic data across different conditions, technologies, and species. *Nat. Biotechnol.* **36**, 411–420 (2018).
- Stuart, T. et al. Comprehensive integration of single-cell data resource comprehensive integration of single-cell data. *Cell* **177**, 1888–1902 (2019).
- Hafemeister, C. & Satija, R. Normalization and variance stabilization of single-cell RNA-seq data using regularized negative binomial regression. *Genome Biol.* **20**, 296 (2019).
- Subramanian, A. et al. Gene set enrichment analysis: a knowledge-based approach for interpreting genome-wide expression profiles. *Proc. Natl Acad. Sci. USA* **102**, 15545–15550 (2005).
- Liberzon, A. et al. Molecular Signatures Database (MSigDB) 3.0. *Bioinformatics* **27**, 1739–1740 (2011).
- Linderman, G. C., Zhao, J. & Kluger, Y. Zero-preserving imputation of scRNA-seq data using low-rank approximation. Preprint at *bioRxiv* <https://doi.org/10.1101/397588> (2018).

Acknowledgements

We are grateful for the valuable assistance of the staff of the flow cytometry, bioimaging and animal facilities at our institutions. We thank J.-W. Taanman, A. Magalhães, J. Ribot, K. Serre and N. Sousa for technical suggestions and administrative help. This work was supported by the Wellcome Trust (092973/Z/10/Z to D.J.P.), Biotechnology and Biological Sciences Research Council (BBSRC) UK (BB/R017808/1 to D.J.P.), European Research Council (ERC) under the European Union's Horizon 2020 research and innovation programme (grant agreement no. 646701 to B.S.-S.; StG_679173 to L.L.), Science Foundation Ireland (SFI) (16/FRL/3865 to L.L.), NIH (NS115064, HG008155, AG062377 to M.K.), NIH (R01 AI134861 and metabolic core grant S10 OD020100 to L.L.), Fundação Astrazeneca (Prémio FAZ Ciência 2019 to B.S.-S. and N.L.) and PAC-PRECISE LISBOA-01-0145-FEDER-016394, co-funded by FEDER (POR Lisboa 2020 (Programa Operacional Regional de Lisboa, do Portugal 2020)) and Fundação para a Ciência e a Tecnologia (Portugal). N.L. is supported by a postdoctoral fellowship from EMBO (ALTF 752-2018); S.M. was supported by a studentship from the Medical Research Council (MRC) UK; G.F. is supported by the European Union's Horizon 2020 research and innovation programme under the Marie Skłodowska-Curie grant agreement no. 752932; and A.D., S.C., L.D. and H.P. are supported by Irish Research Council fellowships.

Author contributions

N.L., C.M., S.M. and M.R. performed most of the experiments and analyzed the data. G.J.F. designed and performed some experiments. N.S., A.C.K., L.D., H.K., A.D., S.C.,

H.P., R.L. and C.C. provided technical assistance in some experiments. M.K. and L.Z.A. performed bioinformatic analysis, and M.B. provided reagents, materials and support. P.P. and R.J.A. provided key assistance with the SCENITH™ methodology. B.S.-S., D.J.P. and L.L. conceived and supervised the study. N.L., C.M., B.S.-S., D.J.P. and L.L. wrote the manuscript.

Competing interests

B.S.-S. is an inventor of the patented 'Delta One T cell' technology, which has been acquired by GammaDelta Therapeutics (London, UK).

Additional information

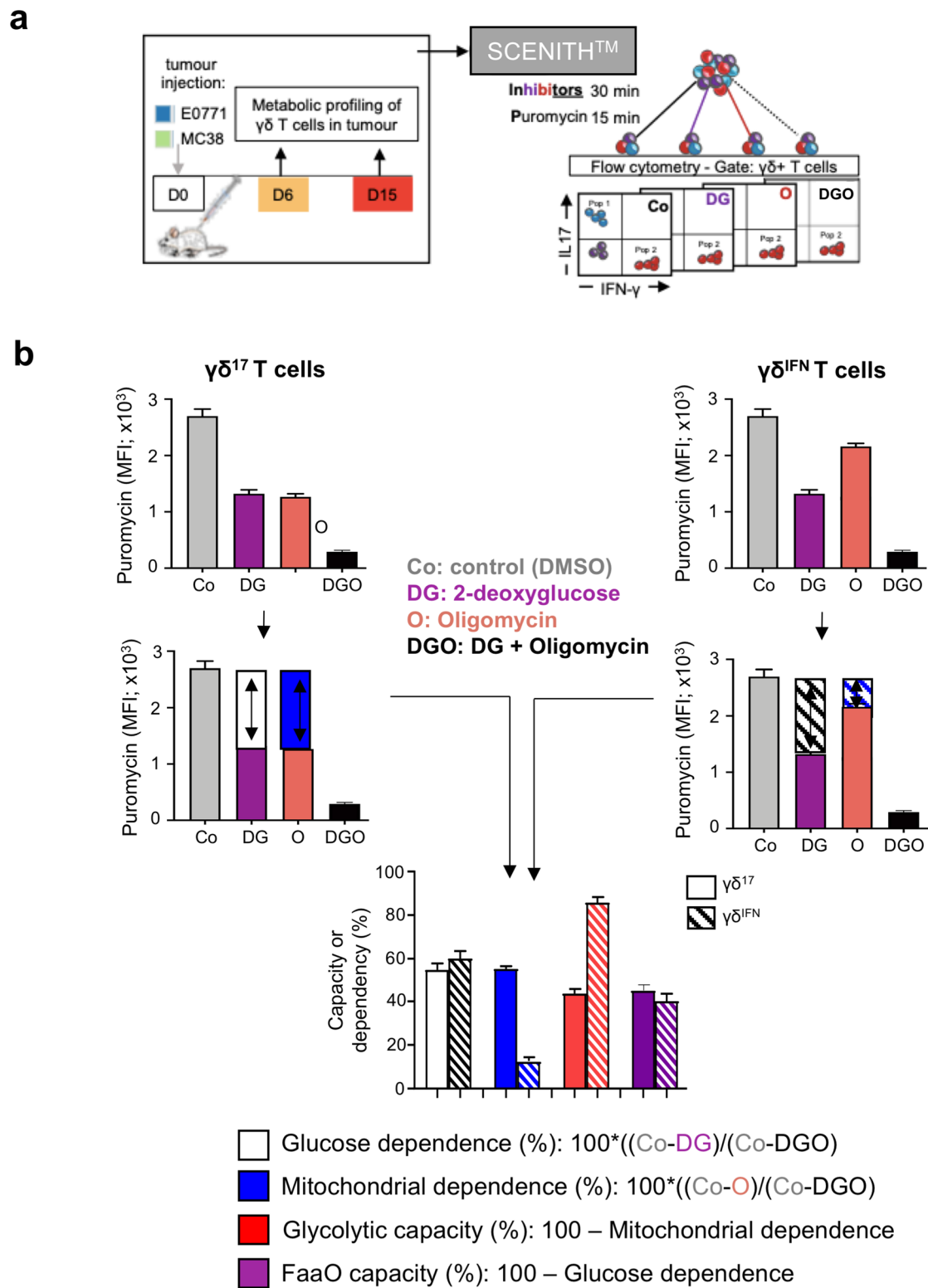
Extended data is available for this paper at <https://doi.org/10.1038/s41590-020-00848-3>.

Supplementary information is available for this paper at <https://doi.org/10.1038/s41590-020-00848-3>.

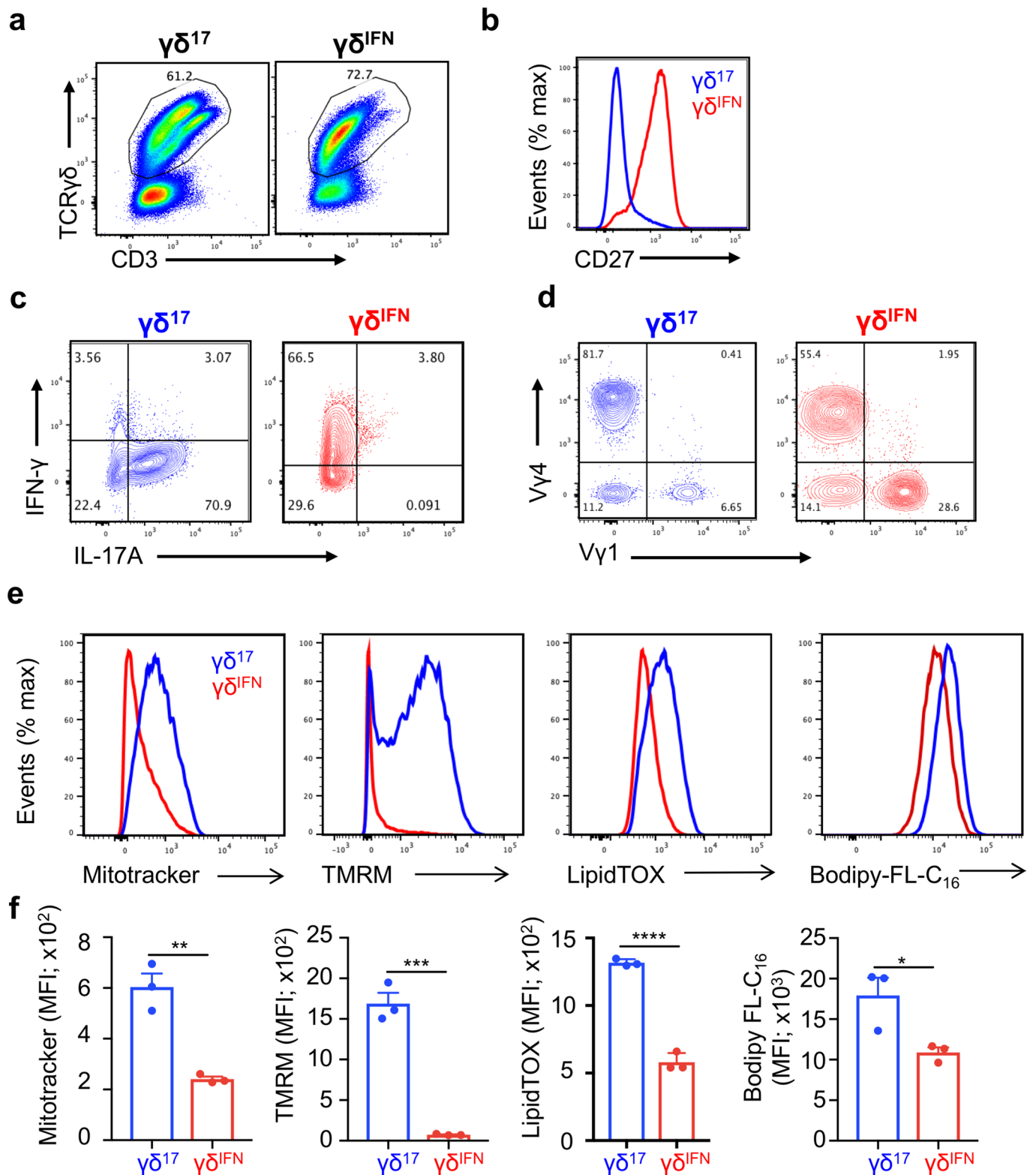
Correspondence and requests for materials should be addressed to D.J.P.

Peer review information *Nature Immunology* thanks Juan Carlos Zúñiga-Pflücker and the other, anonymous, reviewer(s) for their contribution to the peer review of this work. Peer reviewer reports are available.

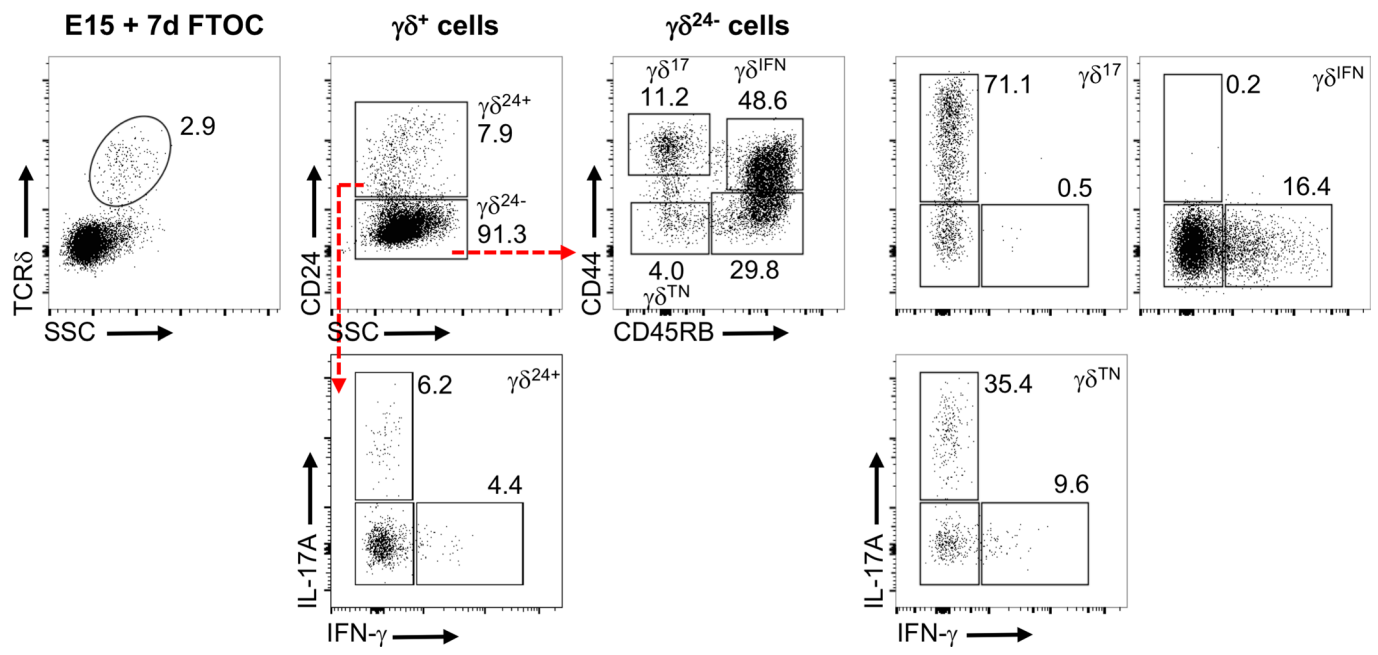
Reprints and permissions information is available at www.nature.com/reprints.



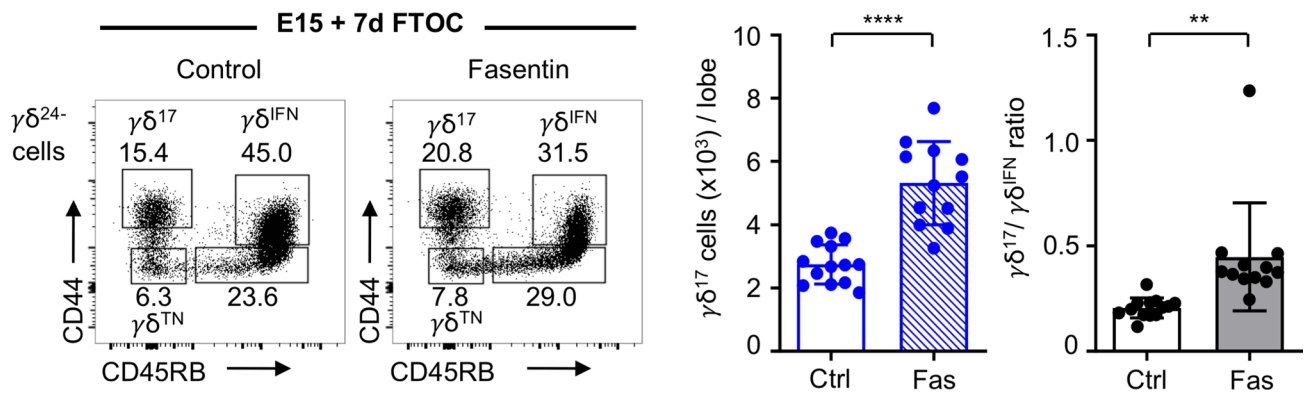
Extended Data Fig. 1 | SCENITH™ methodology for analysis of cell metabolism. **a**, Experimental design: E0771 breast or MC38 colon cancer cell lines were injected in WT mice; 6 and 15 days later, tumors were extracted for metabolic analysis of gd T cells using SCENITH™. **b**, SCENITH™ assesses the impact of metabolic inhibitors on protein synthesis. Mean fluorescence intensity (MFI) of puromycin is analysed in each condition (Co: control-no inhibition; DG: 2-deoxyglucose inhibiting glycolysis; O: oligomycin inhibiting OXPHOS; and DGO: DG+O inhibitors). Glucose dependence, fatty acid and amino acid oxidation capacity, mitochondrial dependence and glycolytic capacity are calculated as detailed in the Methods and reference #23. Error bars show mean+SEM. Data are representative of 3 independent experiments (n=3 mice in triplicates per group and per experiment).



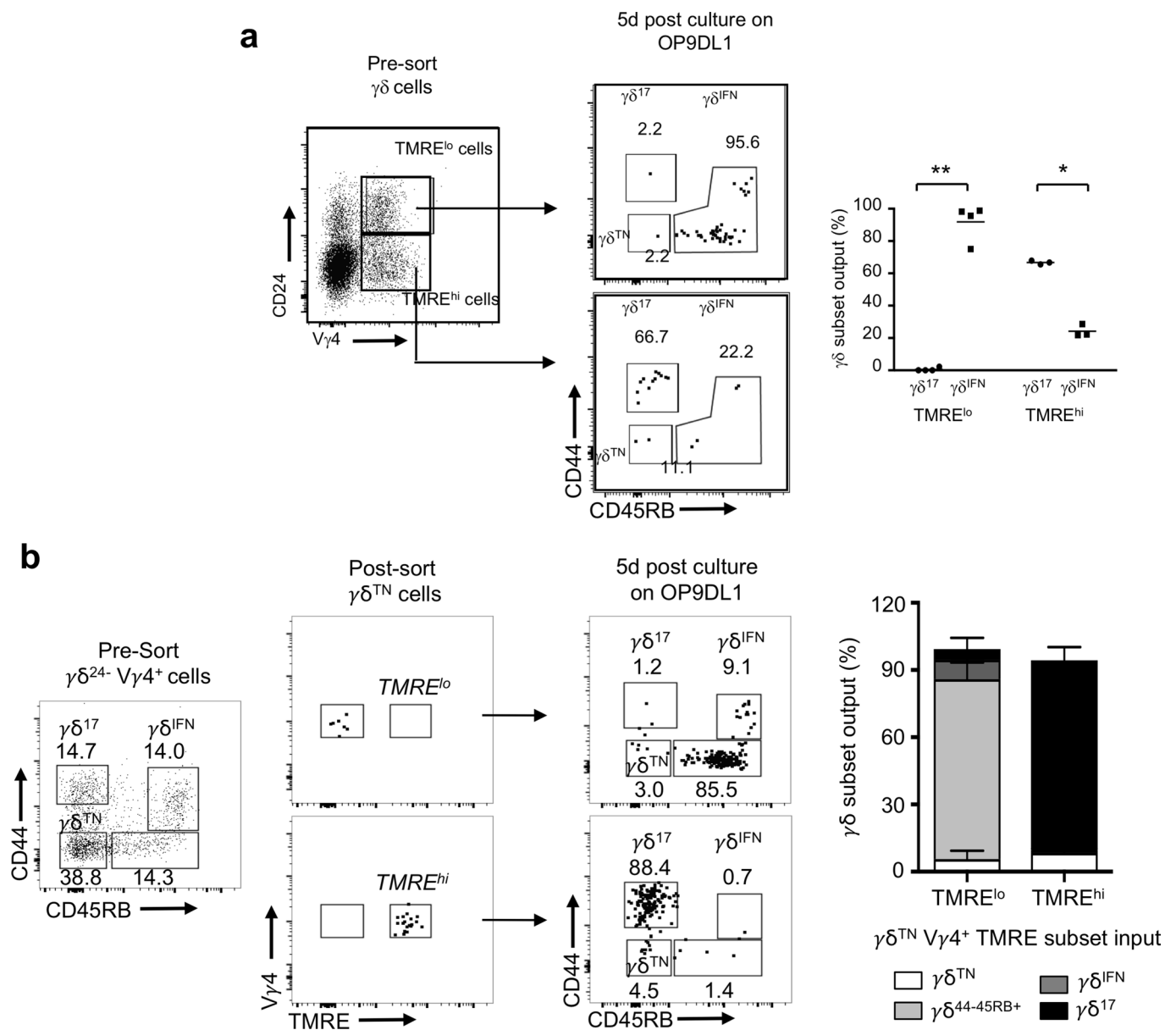
Extended Data Fig. 2 | In vitro expanded $\gamma\delta^{17}$ and $\gamma\delta^{IFN}$ $\gamma\delta$ T cells retain their mitochondrial and lipid phenotypes. **a**, Representative flow plots of CD3 and TCR $\gamma\delta$ expression on $\gamma\delta^{17}$ and $\gamma\delta^{IFN}$ T cells expanded in vitro from total spleen/LN cells. **b**, CD27 expression on in vitro expanded $\gamma\delta^{17}$ and $\gamma\delta^{IFN}$ $\gamma\delta$ T cells. **c**, IL-17 and IFN γ production by in vitro expanded $\gamma\delta^{17}$ and $\gamma\delta^{IFN}$ T cells respectively, following activation with PMA/ionomycin. **d**, V γ 1 and V γ 4 expression on in vitro expanded $\gamma\delta^{17}$ and $\gamma\delta^{IFN}$ T cells. **e**, Representative staining of in vitro expanded $\gamma\delta^{17}$ and $\gamma\delta^{IFN}$ T cells for mitotracker, TMRM, lipidTOX and Bodipy-FL-C₁₆. **f**, MFI of mitotracker, TMRM, lipidTOX and Bodipy-FL-C₁₆ staining in vitro expanded $\gamma\delta^{17}$ and $\gamma\delta^{IFN}$ T cells. $n=3$, data representative of 3 independent experiments. Mitotracker $p=0.0026$; TMRM $p=0.0003$; LipidTOX $p<0.0001$; Bodipy-FL-C₁₆ $p=0.036$. Error bars show mean+SD, ** $p<0.01$, *** $p<0.001$, **** $p<0.0001$, using two-tailed unpaired Student's t -test.



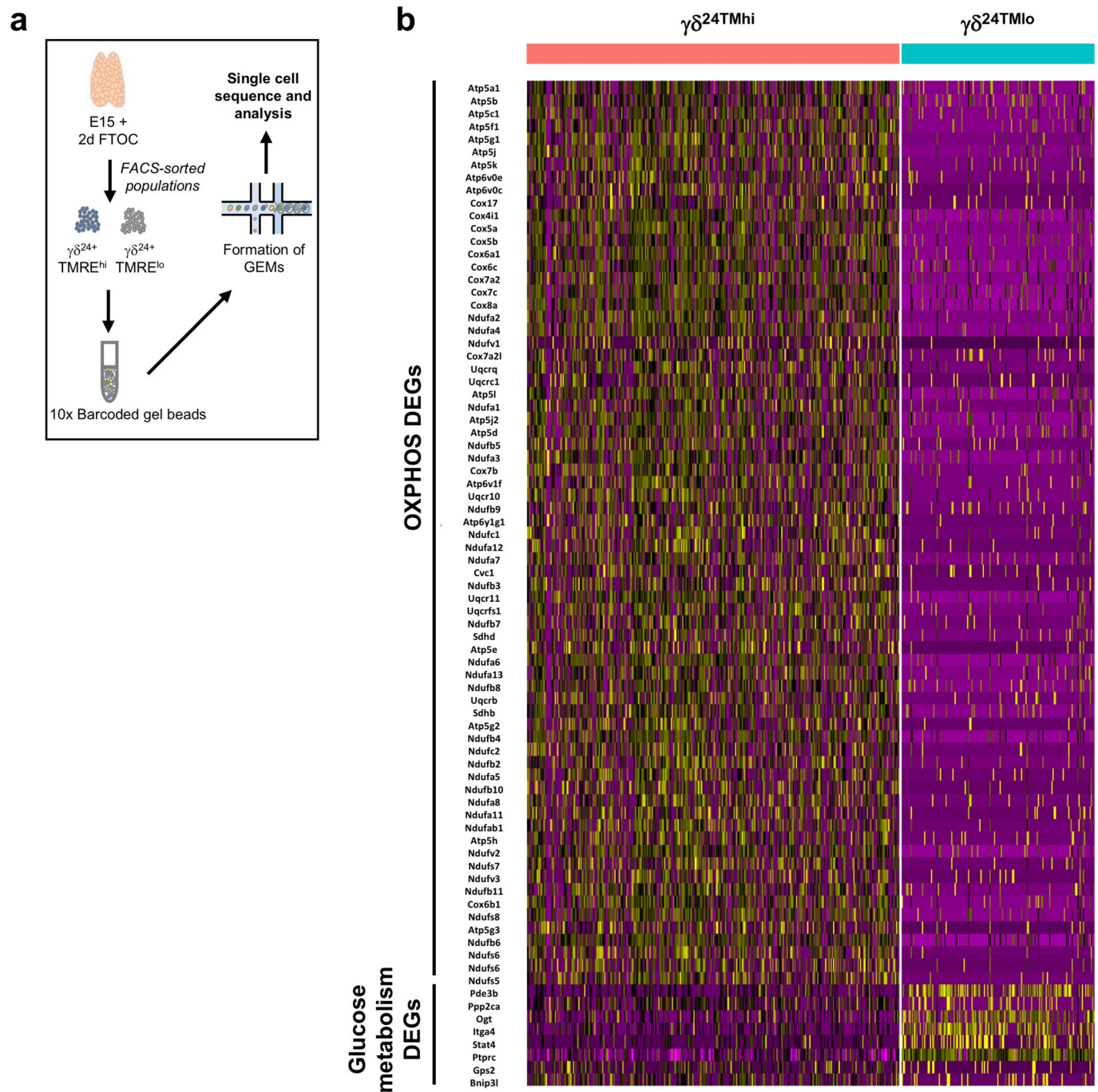
Extended Data Fig. 3 | $\gamma\delta^{TN}$ cells can generate $\gamma\delta^{17}$ and $\gamma\delta^{IFN}$ T cells. Flow cytometry profiles of thymic $\gamma\delta$ T cells from E15 thymic lobes that had been cultured for 7-days in fetal thymic organ culture (E15 + 7dFTOC). CD24⁺ ($\gamma\delta^{24+}$) precursors downregulate CD24 to become a CD24⁻CD44⁺CD45RB⁻ ($\gamma\delta^{TN}$) population. $\gamma\delta^{TN}$ cells are able to become either IL-17-secreting CD44⁺CD45RB⁻ $\gamma\delta^{17}$ cells, or IFN- γ -producing CD44⁺CD45RB⁺ $\gamma\delta^{IFN}$ cells.



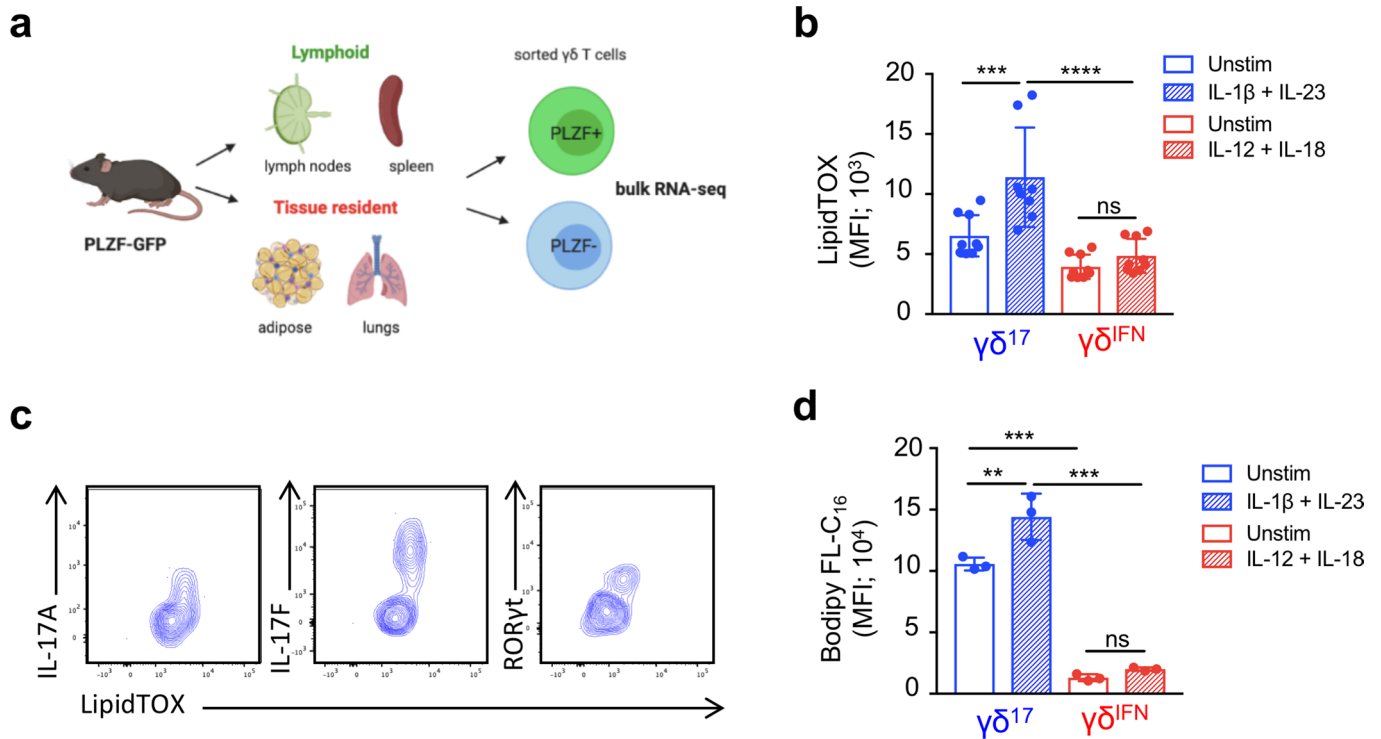
Extended Data Fig. 4 | Thymic $\gamma\delta^{17}$ cells are increased upon inhibition of glucose uptake. Flow cytometry profiles of thymic $\gamma\delta^{TN}$ ($CD44^-CD45RB^-$), $\gamma\delta^{17}$ ($CD44^+CD45RB^-$) and $\gamma\delta^{IFN}$ ($CD44^+CD45RB^+$) cells in $\gamma\delta^{24-}$ cells from E15 thymic lobes in 7-day FTOC with media containing or not Fasentin. Histograms show the number of $\gamma\delta^{17}$ T cells ($p < 0.0001$) and $\gamma\delta^{17}/\gamma\delta^{IFN}$ ratio ($p = 0.0028$). Data are representative of 2 independent experiments (at least 4 lobes pooled per group per experiment). Error bars show mean \pm SEM, ** $p < 0.01$, **** $p < 0.0001$, using two-tailed unpaired Student's t-test.



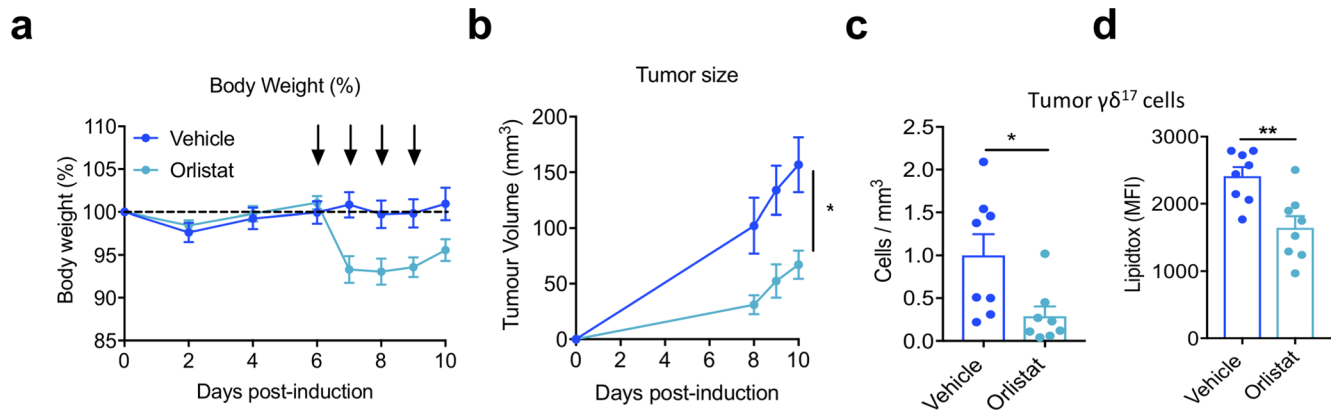
Extended Data Fig. 5 | Mitochondrial activity identifies V γ 4⁺ progenitors with distinct effector fates at very early stages. a, Flow cytometry plots pre-sort, and after sorted TMRE^{lo} and TMRE^{hi} V γ 4⁺ $\gamma\delta$ 24⁺ cells were cultured for 5-days on OP9DL1 cells. Percentage of thymic $\gamma\delta^{17}$ and $\gamma\delta^{IFN}$ cells generated are displayed in the graph on right. Data are representative of 3 independent experiments (cells sorted from $n = 4$ independent mice pooled per group per experiment). **b**, Flow cytometry plots for pre- and post-sort TMRE^{hi} and TMRE^{lo} V γ 4⁺ $\gamma\delta^{TN}$ cells that were cultured on OP9-DL1 cells for a further 5-days (plots on right). Histogram shows the percentage of each $\gamma\delta$ T cell subset generated from cultured TMRE^{lo} and TMRE^{hi} V γ 4⁺ $\gamma\delta^{TN}$ cells. Error bars show mean + SD. Data are representative of 2 independent experiments (at least 4 lobes pooled per group per experiment). Error bars show mean \pm SD, * $p < 0.05$, *** $p < 0.01$, using two-tailed unpaired Student's t -test.



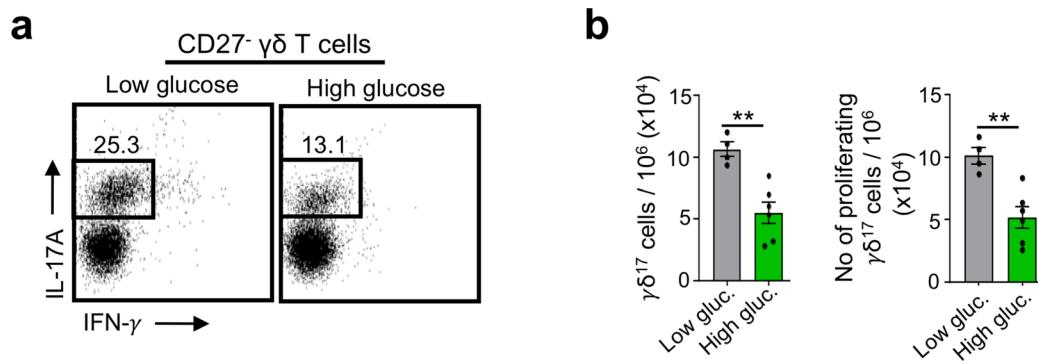
Extended Data Fig. 6 | Distinct mitochondrial activities underlie effector fate of thymic $\gamma\delta$ T cell progenitors. **a**, Experimental design for single-cell RNAseq (10x Genomics) on TMRE^{lo} and TMRE^{hi} $\gamma\delta^{24+}$ cells from E15 + 2d FTOC. **b**, Heatmap of differentially upregulated genes from comparison of TMRE^{lo} and TMRE^{hi} $\gamma\delta^{24+}$ cells. Genes are grouped in relation to their function in either OxPhos or glucose metabolism.



Extended Data Fig. 7 | Enriched lipid metabolism and higher lipid uptake in $\gamma\delta^{17}$ cells. **a**, Experimental set up for bulk RNA-sequencing of PLZF⁺ (gd^{17}) and PLZF⁻ (gd^{IFN}) cells isolated from PLZF-GFP (*Zbtb16*^{GFP}) mice. **b**, LipidTOX MFI in $\gamma\delta^{17}$ (CD27⁺) and $\gamma\delta^{IFN}$ (CD27⁺) T cells from LN cells activated in vitro with IL-1 β +IL-23 and IL-12+IL-18 respectively. n=9, data pooled from 3 independent experiments. **c**, Representative plots of LipidTOX staining and IL-17A, IL-17F or ROR γ t expression in $\gamma\delta^{27-}$ T cells from LNs activated in vitro with IL-1 β +IL-23 for 6h. Data representative of 3 independent experiments. **d**, Bodipy-FL-C₁₆ MFI in $\gamma\delta^{17}$ (CD27⁺) and $\gamma\delta^{IFN}$ (CD27⁺) T cells T cells unstimulated or stimulated in vitro with IL-12+IL-18 or IL-1 β +IL-23. (n=3, data from 1 experiment; $\gamma\delta^{17}$ p=0.0044; $\gamma\delta^{IFN}$ p=0.8035). Error bars show mean+SD, **p < 0.01, ***p < 0.001, ****p < 0.0001 using one-way ANOVA.



Extended Data Fig. 8 | Inhibition of dietary fat uptake reduces tumour growth and $\gamma\delta^{17}$ cells in the tumour. B16F10-tumour bearing mice were given daily injections of either vehicle or orlistat on days 6-9, and tumours were analysed on day 10. **a**, Percentage body weight following tumor cell injection; arrows indicate when orlistat or vehicle were administered. **b**, Tumor volume on days 8-10 following B16F10 inoculation. Absolute numbers **c**, and LipidTOX staining **d**, of tumor-infiltrating $\gamma\delta^{17}$ cells on day 10. $n=8$ biologically independent animals, data from 1 independent experiment. Data represents mean+SD, * $p<0.06$, ** $p<0.01$ using unpaired Student's t-test or one-way ANOVA.



Extended Data Fig. 9 | Glucose supplementation diminishes $\gamma\delta^{17}$ cell numbers and proliferation. **a**, Flow cytometry profiles of peripheral $\gamma\delta^{17}$ T cells cultured with media containing low (5mM) or high (50mM) doses of glucose. Graph depicts total numbers of $\gamma\delta^{17}$ T cells ($p=0.0028$). **b**, Number of proliferating Ki-67⁺ $\gamma\delta^{17}$ T cells cultured with low or high glucose ($p=0.0034$). $n=6$ biologically independent animals, data from 2 independent experiments. Error bars show mean \pm SEM, ** $p < 0.01$, using unpaired two-tailed Student's t-test.

Reporting Summary

Nature Research wishes to improve the reproducibility of the work that we publish. This form provides structure for consistency and transparency in reporting. For further information on Nature Research policies, see [Authors & Referees](#) and the [Editorial Policy Checklist](#).

Statistics

For all statistical analyses, confirm that the following items are present in the figure legend, table legend, main text, or Methods section.

n/a Confirmed

- The exact sample size (n) for each experimental group/condition, given as a discrete number and unit of measurement
- A statement on whether measurements were taken from distinct samples or whether the same sample was measured repeatedly
- The statistical test(s) used AND whether they are one- or two-sided
Only common tests should be described solely by name; describe more complex techniques in the Methods section.
- A description of all covariates tested
- A description of any assumptions or corrections, such as tests of normality and adjustment for multiple comparisons
- A full description of the statistical parameters including central tendency (e.g. means) or other basic estimates (e.g. regression coefficient) AND variation (e.g. standard deviation) or associated estimates of uncertainty (e.g. confidence intervals)
- For null hypothesis testing, the test statistic (e.g. F , t , r) with confidence intervals, effect sizes, degrees of freedom and P value noted
Give P values as exact values whenever suitable.
- For Bayesian analysis, information on the choice of priors and Markov chain Monte Carlo settings
- For hierarchical and complex designs, identification of the appropriate level for tests and full reporting of outcomes
- Estimates of effect sizes (e.g. Cohen's d , Pearson's r), indicating how they were calculated

Our web collection on [statistics for biologists](#) contains articles on many of the points above.

Software and code

Policy information about [availability of computer code](#)

Data collection

Flow cytometry data was acquired using BD FACSDiva software (BD Bioscience).
Seahorse metabolic flux data was collected using XFe-96 / Seahorse XFp analyser softwares (Seahorse Bioscience).
Imaging data was collected using INSPIRE acquisition software (Amnis) and Zen 2.3 software (Zeiss).
CLAMS data was collected using metascreen (Sable Systems)
For triglyceride quantification data was collected using FLUOstar OPTIMA (BMG Labtech)

Data analysis

All analysis were described in the relevant section of Methods.
Flow cytometry data was analysed using FlowJo v10 software.
Seahorse metabolic flux data was analysed using Seahorse XFp analyser software (Seahorse Bioscience).
Imaging data was analysed using IDEAS software (Amnis) and ImageJ version 2.0.0.
Single-cell RNAseq data was analysed using the R package Seurat v2.3.
Cufflinks and Cuffdiff was used for bulk RNA sequencing analysis.
CLAMS data was analysed using EpeData (Sable Systems) and CaIR Version 1.2 (doi: <http://www.sciencedirect.com/science/article/pii/S1550413118304017>)
Statistical analysis were done with GraphPad Prism 8.4.2

For manuscripts utilizing custom algorithms or software that are central to the research but not yet described in published literature, software must be made available to editors/reviewers. We strongly encourage code deposition in a community repository (e.g. GitHub). See the Nature Research [guidelines for submitting code & software](#) for further information.

Data

Policy information about [availability of data](#)

All manuscripts must include a [data availability statement](#). This statement should provide the following information, where applicable:

- Accession codes, unique identifiers, or web links for publicly available datasets
- A list of figures that have associated raw data
- A description of any restrictions on data availability

The accession code for single cell RNA sequencing data is GSE150585 and for bulk RNA sequencing data is GSE156782

Field-specific reporting

Please select the one below that is the best fit for your research. If you are not sure, read the appropriate sections before making your selection.

- Life sciences Behavioural & social sciences Ecological, evolutionary & environmental sciences

For a reference copy of the document with all sections, see [nature.com/documents/nr-reporting-summary-flat.pdf](https://www.nature.com/documents/nr-reporting-summary-flat.pdf)

Life sciences study design

All studies must disclose on these points even when the disclosure is negative.

Sample size	No sample size calculation were performed. Pilot studies were used for estimation of the sample size required. In some instances, three replicates had to be performed due to the larger signal-to-noise ratio, while conclusions could be made from other experiments where variability was less.
Data exclusions	Obvious outliers were excluded. We also excluded data from failed experiments. Data exclusions concern SCENITH experiments and in vitro experiments.
Replication	All experiments were reproduced to reliably support conclusions stated in the manuscript. Each experiment was repeated in multiple animal and at least twice unless otherwise stated.
Randomization	Samples were randomly allocated into a control or experimental group. In the B16 tumor model, mice were randomized into groups after tumor cell injection.
Blinding	No blinding was used. However, the outcomes were measured as objective as possible. We also performed duplicates, triplicates and we repeated experiments many times to limited biases introduced by the lack of blinding.

Reporting for specific materials, systems and methods

We require information from authors about some types of materials, experimental systems and methods used in many studies. Here, indicate whether each material, system or method listed is relevant to your study. If you are not sure if a list item applies to your research, read the appropriate section before selecting a response.

Materials & experimental systems

n/a	Involvement in the study
<input type="checkbox"/>	<input checked="" type="checkbox"/> Antibodies
<input type="checkbox"/>	<input checked="" type="checkbox"/> Eukaryotic cell lines
<input checked="" type="checkbox"/>	<input type="checkbox"/> Palaeontology
<input type="checkbox"/>	<input checked="" type="checkbox"/> Animals and other organisms
<input checked="" type="checkbox"/>	<input type="checkbox"/> Human research participants
<input checked="" type="checkbox"/>	<input type="checkbox"/> Clinical data

Methods

n/a	Involvement in the study
<input checked="" type="checkbox"/>	<input type="checkbox"/> ChIP-seq
<input type="checkbox"/>	<input checked="" type="checkbox"/> Flow cytometry
<input checked="" type="checkbox"/>	<input type="checkbox"/> MRI-based neuroimaging

Antibodies

Antibodies used

From eBioscience - Anti-CD3ε (145-2C11) #78-0031-82, CD24 (M1/69) #48-0242-82, CD25 (PC61) #25-0251-82, CD27 (LG.7F9) #11-0271-82, CD73 (TY/11.8) 25-0731-82, Vy2 (UC3-10A6) #25-5828-82, IFNγ (XMG1.2) #12-7311-41, Ki-67 (SolA15) #56-5698-82, RORyt (B2D) #25-6981-82, TCRδ (GL3) #17-5711-82 and Tbet (4B10) #17-5825-82

From BD Bioscience - Anti-CD44 (IM7) #560569, anti-CD16/32 (2.4G2) #553140

From Biolegend - Anti-TCRδ (GL3) #118119, CD45RB (C363.16A) #103319, CD45 (30-F11) #103149, Vy1 (2.11) #141107, Vy4 (UC3-10A6) #137711, Vy5 (536) #137505 and CD24 (M1/69) #101815, IL-17F (9D3.1C8) #517004, IL-17A (TC11-18H10.1) #506929, CD16/32 (Trustain) #101320

Validation

The antibodies used in this study were used according to the manufacturer's recommendation.

Eukaryotic cell lines

Policy information about [cell lines](#)

Cell line source(s)

The E0771 murine breast adenocarcinoma cancer cells, MC38 murine colon adenocarcinoma cells and B16.F10 melanoma cells were purchased from ATCC (Manassas, VA).

Authentication

None of the cell lines used were authenticated

Mycoplasma contamination

All cell lines are tested negative for mycoplasma contamination

Commonly misidentified lines
(See [ICLAC](#) register)

Name any commonly misidentified cell lines used in the study and provide a rationale for their use.

Animals and other organisms

Policy information about [studies involving animals](#); [ARRIVE guidelines](#) recommended for reporting animal research

Laboratory animals

C57Bl/6J WT mice and Myc-GFP mice (B6;129-Myctm1Slek/J) were purchased from Charles River and Jackson Laboratories. PLZF-GFP (Zbtb16GFP) mice were generated in the laboratory of Dr. Sant'Angelo with a modified bacterial artificial chromosome transgene expressing eGFP under the control of PLZF regulatory elements. Males and females were used at the foetal (embryonic day 14-18), neonatal (1-5 days old) or adult (6-12 weeks) stages. Mice were housed in 12-hour/12-hour light/dark cycle at an ambient temperature of 22+/- 1°C with humidity 52-55%.

Wild animals

No wild animals were used in the study.

Field-collected samples

No field samples were collected in the study.

Ethics oversight

All mouse experiments performed in this study were evaluated and approved by the institutional ethical committee (Instituto de Medicina Molecular Orbea), the national competent authority (DGAV) under the license number 019069, UK Home Office regulations and institutional guidelines under license number 70/8758 and by the Institutional Animal Care and Use Committee of Brigham and Women's Hospital and Harvard Medical School, the Trinity College Dublin ethics committee.

Note that full information on the approval of the study protocol must also be provided in the manuscript.

Flow Cytometry

Plots

Confirm that:

- The axis labels state the marker and fluorochrome used (e.g. CD4-FITC).
- The axis scales are clearly visible. Include numbers along axes only for bottom left plot of group (a 'group' is an analysis of identical markers).
- All plots are contour plots with outliers or pseudocolor plots.
- A numerical value for number of cells or percentage (with statistics) is provided.

Methodology

Sample preparation

Tumours were collected and digested with 1mg/mL collagenase Type I, 0.4mg/mL collagenase Type IV (Worthington) and 10 µg/mL DNase I (Sigma-Aldrich) for 30 minutes at 37 C. Cell suspension was then filtered through a 100 µm nylon cell strainer (Falcon/Corning). γδ T cells were isolated by scratching thymus, spleen and lymph node on a 70µm mesh. Lungs were minced then homogenized in RPMI 1640 using a TissueLyser (Qiagen) and filtered through 70µm wire mesh. Adipose tissue was processed as described previously (3). Red blood cells were lysed using RBC Lysis Buffer (Biolegend) or ammonium chloride lysis buffer (made in-house). Single-cell suspensions of foetal and neonatal thymocytes were obtained by gently homogenizing thymic lobes followed by straining through 40µm strainers (BD).

Cells were incubated for 15 min at 4°C with Fc-block (anti-CD16/CD32, 2.4G2, BD biosciences) before surface staining. For intracellular staining, cells were fixed, permeabilized and stained with the Foxp3 staining kit or with BD Cytofix/Cytoperm and Perm/Wash buffers.

Instrument

Sorts were performed using a FACS AriaIII cell sorter (BD) and analysis were done with Fortessa, LSRII or Cantoll (BD Biosciences)

Software

Flow cytometry data was collected using BD FACSDiva software (BD Bioscience) and analysed using FlowJo software.

Cell population abundance

Post-sort sample purity was examined by flow cytometry. Samples containing at least 95% of desired population were used for further analysis.

Gating strategy

Using the FSC/SSC, debris were removed. We excluded doublet by using FSC-A/FSC-H and SSC-A/SSC-H. We used viability dye.

Gating strategy

Positive threshold was applied to all samples within cell populations. $\gamma\delta$ T cells are defined as CD3+TCR δ +. $\gamma\delta$ IFN were gated on CD27+, IFN γ + or CD44+CD45RB+. $\gamma\delta$ 17 were gated on CD27-, IL-17+ or CD44+CD45RB-.

Tick this box to confirm that a figure exemplifying the gating strategy is provided in the Supplementary Information.